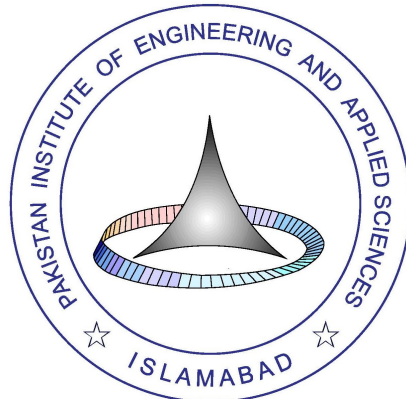


Generation, Stabilization, and Manipulation of Kerr Cat States in Superconducting Resonators



Muhammad Shuraim

Submitted in partial fulfillment of the requirements
for the degree of BS Physics.

2023

Department of Physics and Applied Mathematics
Pakistan Institute of Engineering and Applied Sciences
Nilore, Islamabad, Pakistan

This page is intentionally left blank.

Certificate of Approval

This is to certify that the work contained in this thesis entitled **Generation, Stabilization, and Manipulation of Kerr Cat States in Superconducting Resonators**, was carried out by **Muhammad Shuraim**, and in my opinion, it is fully adequate, in scope and quality, for the degree of **Bachelors**. Furthermore, it is hereby approved for submission for review and thesis defense.

Supervisor: _____

Name: **Dr. Muhammad Irfan**
Date: 04 July 2023
Place: PIEAS, Islamabad

Co-Supervisor: _____

Name: **Dr. Shahid Qamar**
Date: 04 July 2023
Place: PIEAS, Islamabad

Head, DPAM: _____

Name: **Dr Shakeel ur Rahman**
Date: 04 July 2023
Place: PIEAS, Islamabad

Dedications

Dedicated to my father, mother, and only good mentors :-y

Declaration of Originality

I hereby declare that the work contained in this thesis and the intellectual content of this thesis are the product of my work. This thesis has not been previously published in any form nor does it contain any verbatim of the published resources which could be treated as infringement of the international copyright law. I also declare that I do understand the terms ‘copyright’ and ‘plagiarism,’ and that in case of any copyright violation or plagiarism found in this work, I will be held fully responsible for the consequences of any such violation.

Muhammad Shuraim

Date: 04 July 2023

Place: PIEAS, Islamabad

Acknowledgments

There are many people that have made my bachelor's dissertation, an excellent culmination of my BS in Physics at the Pakistan Institute of Engineering and Applied Sciences. While I cannot list them all here, I especially wish to THANK

- Dr. Muhammad Irfan, my esteemed supervisor, has played a pivotal role in my academic journey, often transcending the boundaries of a typical supervisor-student relationship to become a friend. His expert guidance and mentorship have significantly enhanced my research skills, making my bachelor's dissertation an immensely enjoyable and fulfilling experience.
- Dr. Muhammad Waseem, an informative and hardworking physicist, always have with him the finest discussions.
- Dr. Amrendra Kumar Surma and Dr. Carlos Navarrete-Benlloch, helped me a lot with Quantum Optics concepts. Dr. Steven Girvin and Dr. Andreas Wallraff whose online help and lecture notes remain a significant source of valuable knowledge.
- Dr. Shahid Qamar, co-supervisor although (but sadly) can't have any discussion regarding my project due to his business being Pro-Rector.
- Dr. Shakeel ur Rahman, a nice person and current HOD. Dr. Aftab Rafiq, ex-HOD, always motivates me and is useful in terms of career planning.
- Dr. Muhammad Ali, French teacher and useful in terms of living a good life.
- Dr. Yousuf Hamza, a very nice teacher, with good pedagogical skills.
- Dr. Zaheer Asghar, always has useful discussions.
- Muhammad Haroon, the very first person who made me well-acquainted with quantum optics experiments and interests in this field.
- Dr. Ishtiaq, who has helped me/us(Danians) a lot in the matters of finance management.
- Meesum bhai, my friends and classmates (BSPhy'PIEAS, 19-23) especially Saad, Marguerite, et al.
- et alia

Merci beaucoup!

Copyrights Statement

The entire contents of this thesis entitled **Generation, Stabilization, and Manipulation of Kerr Cat States in Superconducting Resonators** by **Muhammad Shuraim** are an intellectual property of Pakistan Institute of Engineering and Applied Sciences (PIEAS). No portion of the thesis should be reproduced without obtaining explicit permission from PIEAS.

Contents

1	Introduction	2
1.1	Thesis Overview	7
2	Two-level System and Field Quantization	8
2.1	Two Level Systems	8
2.2	Classical to Quantum Regime	13
2.2.1	Quantum Harmonic Oscillator	13
2.3	Quantization of Electromagnetic Waves	16
2.3.1	Deriving the Hamiltonian of traveling EM Waves	16
2.3.2	Model the Hamiltonian of stationary EM Waves	17
2.4	Quantum States and its Representation	19
3	Circuit Quantum Electrodynamics	22
3.1	Superconductivity and Cooper Pair Box	23
3.2	Transmission Lines	26
3.2.1	Quantization of transmission lines	28
3.2.2	Model the Hamiltonian of transmission line resonators	31
3.2.3	Cooper Pair Box coupled with external voltage	32
3.3	The Jaynes Cummings (JC) Model	33
3.3.1	Rabi oscillations	36
3.3.2	Dispersive case when $ \Delta \gg g$	37
3.4	Josephson Junctions	38
3.4.1	Flux quantization	39
3.4.2	Nonlinear effects of Josephson junctions	40
3.4.3	Hamiltonian of Josephson Junctions	41
3.5	Types of Superconducting Qubit	42

3.5.1	Charge Qubit	43
3.5.2	Phase Qubit	43
3.5.3	Flux Qubit	44
3.6	Transmon Qubit	44
3.6.1	Hamiltonian of Transmon qubit	45
3.7	Quantum Master Equation	47
3.7.1	QME of Transmon qubit/TLS in the presence of relaxation and dephasing	48
4	A New Approach to Engineer the Kerr-cat States in Superconducting Resonators	50
4.1	Conceptual Overview	50
4.1.1	Kerr effect and the Schrodinger cat states	50
4.2	Model a Hamiltonian of the Kerr-nonlinear Resonator	51
4.2.1	Steady state of the system Hamiltonian	52
4.3	Preparation of Cat States	55
4.3.1	Adiabatic increase of two-photon drive	55
4.3.2	Non-adiabatic initialization of the cat states	56
4.4	Stabilization of Kerr-cat States by using Two-Photon Drive	58
4.5	qcMAP gate	59
4.6	Implementation of Universal Quantum Logic Gates	60
4.6.1	Z gate	60
4.6.2	NOT or X gate	61
4.6.3	Entangling Gate	62
4.7	Circuit Realizations of Two-Photon Driven Kerr-nonlinear Resonator	62
4.8	Conclusion	63
References		64

List of Figures

1.1	Schematics of the general architecture of quantum computing processor containing highly coupled two-level atoms, cavities/resonators, and microwave field.	2
2.1	Plot of E vs E_z when $E_x = 0$ (green curve) and $E_x \neq 0$ (blue curve). For the case when $E_x \neq 0$ then we get a superposition of basis states $P = \frac{1}{\sqrt{2}} (1\rangle)$ and $Q = \frac{1}{\sqrt{2}} (1-1\rangle)$	10
2.2	Rabi flopping: transfer of probabilities from both states happening with a period of $\Omega t = \pi$. $P_g(t)$ (blue) describes the probability of a state being found in the ground state and $P_e(t)$ (orange) describes the excited state probability.	12
2.3	$P_e(t)$ (blue line) is the probability of TLA to be found in the excited state when detuning is zero while $P_e(t)$ (orange line) is the excited state probability as a function of Rabi frequency when there is a factor of detuning.	13
2.4	Schematic of <i>mass – spring</i> system with a spring constant k having frequency $k = \sqrt{m\omega^2}$. Mass m is oscillating around equilibrium position q_0 .	14
2.5	Plot of the quadratic potential $U(x)$ of Q.H.O. and energy levels of the Q.H.O. having a constant energy level difference $\Delta E = E_n - E_{n-1}$	15
2.6	Representation of the standing wave mode of the electric field with the two plane mirrors placed at 0 and z .	18
2.7	Wigner function of the fock state of a harmonic oscillator whose level number 5 is excited. Negative probabilities are the depiction that the state is a quantum state. $Re[\alpha]$ and $Im[\alpha]$ are the corresponding canonically conjugate pairs.	19
2.8	Wigner function of vacuum state of the quantum harmonic oscillator.	21
2.9	Wigner function of coherent state with the amplitude $\alpha = 3$ (real quantity but it can be an imaginary number)	21
3.1	Schematic of the Lamb shift lifting the degeneracy between 2s and 2p and emitting a quantum of light.	22
3.2	Schematic of the field mode being trapped inside the cavity.	22

3.3	Circuit diagram of charge qubit containing a Josephson junction (JJ) and is coupled through an externally applied voltage. One part of the shunted capacitor and JJ makes a superconducting island.	24
3.4	Graph of charging energy versus gate charge keeping the number of Cooper pair fixed at 1, 0, and -1. This graph is made considering the absence of tunneling term. Due to this fact, the degeneracy/crossings happen at various fractional intervals of gate charge. When we include the tunneling terms working as a perturbation, then these crossing becomes avoided crossing the same was happening in the study of a two-level system ref: chapter 2. Here N=1 means there are more Cooper pairs on the upper island and this graph can also be extrapolated for other N's. In the avoided crossings, the lower branch from $N_G = \frac{1}{2}$ to $\frac{3}{2}$ for $N = 1$ worked as a ground state of the system.	25
3.5	Graph of energy levels against the gate charge of Cooper pair box in the presence and absence of Josephson energy. The points A and B correspond to the superposition of given basis states and are equal to $\frac{1}{\sqrt{2}}(11)$ and $\frac{1}{\sqrt{2}}(1-1)$, respectively.	27
3.6	Schematic representation of the discretization of transmission lines into inductor-capacitor oscillators. Inductors are shown on the upper transmission line and the same is the case for the lower line but for the brevity of the analysis, we exclude them.	27
3.7	Transmission lines are discretized into n LC oscillators. Q_n is the amount of charge at the nth node and L is the value of self-inductance in the transmission line. I_n is the amount of current passing through the nth node.	28
3.8	Graph of dispersion relation in the transmission lines. For smaller values of the wave vector, it behaves linearly but at larger wave vector values it becomes almost quadratic. The maximum height of ω_k at $k = \frac{\pi}{2}$ is $\frac{2}{\sqrt{LC}}$	30
3.9	Schematics of the transmission line resonator with the given boundary conditions	31
3.10	Schematic representation of the Cooper Pair Box when it is coupled with single mode microwave field. This field helps to tune the given artificial atom.	34
3.11	Schematic representation of the splitting of the energy levels. $ \downarrow, 1\rangle$ energy level is splitted into two eigenenergies $E_{\pm}^{(1)} = \hbar\omega \pm \hbar g$ with an energy gap = $2\hbar g$. Similarly, the energy level $ \downarrow, 2\rangle$ is further separated to $E_{\pm}^{(2)} = 2\hbar\omega \pm \hbar g\sqrt{2}$ with a gap = $2\sqrt{2}\hbar g$	36
3.12	Graph of Rabi oscillation showing the transition probabilities. The Blue lines represent the transition probabilities at some coupling parameters but the orange line depicts the case when the coupling constant is lowered than the previous and thus, found transition probabilities are having low rates.	37

3.13	Graph representing the relation of frequency of drive field on-chip microwave resonator against the detuning parameter and ω is the bare cavity frequency. Figure elaborates that how atomic frequency gets lifted and shows two peaks due to the shift in the frequency and the details can be seen in Wallraff research work [1].	38
3.14	Josephson Junction, consists of two Superconducting (S.C.) islands (<i>Al</i>) separated by an insulating material, in this case, <i>Al₂O₃</i>	39
3.15	Circuit diagram of Josephson Junction exhibiting the nonlinear inductance with the shunted capacitance. The box containing a cross sign is the circuit symbol for the Josephson junction.	42
3.16	Representation of the nonlinear energy levels of Josephson junction on the position-dependent potential. The first two energy levels are considered as a two-level atom. The lowest and upper levels correspond to the ground and excited states, respectively.	43
3.17	Circuit diagram of charge qubit/cooper pair box containing one Josephson junction and tuned through an external voltage.	43
3.18	Circuit diagram of phase qubit containing a Josephson junction element with an external electrical current source	44
3.19	Circuit diagram of flux qubit containing three JJ and is coupled with the external magnetic field (into the page).	44
3.20	Representation of the transmon qubit on a superconducting chip having an array-like structure (right). Left is the details of the connection of the circuit components.	45
3.21	Graph representing the linear harmonic term $\{\frac{\Phi_J^2}{2L_J}\}$ - blue line} and nonlinear parts $\{-E_J \cos\left(\frac{\Phi_J}{\Phi_o}\right)\}$ - red line} in the energy description of the transmon qubit.	46
3.22	Schematic portrayal of artificial atom (two-level system here, transmon qubit) in presence of relaxation rate = r_- , dephasing rate = r_ϕ , and transition rate due thermal vibration = r_-	48
4.1	Cavity containing a transmon qubit that induces a Kerr nonlinearity in the system. The frequency of the photon drive is double the frequency of the resonator.	51
4.2	Wigner function of the steady state of the H_{eff} with $E_p = 16\chi$ where $\chi > 0$	54
4.3	Wigner function of the steady state of the H_{eff} with $E_p = 4\chi$ where $\chi < 0$	55
4.4	Wigner function of the cat states when \hat{H}_{2ph} of the system is evolved taking the cavity state as an initial state. The plot is taken at a time, $t = 6.5/\chi$	56

4.5	Wigner function of the cat states when \hat{H}_{2ph} of the system is evolved taking the cavity state as an initial state. The plot is taken at $time = 6.5/\chi$ and $\frac{\chi}{\kappa} = 250$.	56
4.6	Wigner function of the state taken at time $= t = 1.37 \cdot \tau$ where $\tau = 1/\chi$. The final state is achieved when the initial state is a cavity vacuum state evolved through the H_{2ph} .	57
4.7	Wigner function of the state taken at time $t = 1.49\tau$ where $\tau = 1/\chi$. The state is achieved when the initial state is a cavity vacuum state evolved through the $H_{xy} = H_{2ph} + H'$. We have taken one additional drive field $E'_p = i \frac{\dot{\beta}_o(t)}{N_{\beta_o(t)}^{-}[1+2\beta_o(t)]}$ which is realization to H' . Here, the amplitude of coherent state $\beta_o = \sqrt{E_p/\chi}$.	58
4.8	Wigner function of the states at different time scales under lossy KNR Hamiltonian. Initial state: even parity cat states $C_{\beta_o}^+$. Here x-axis = $\text{Re}[\beta_o]$ and y-axis = $\text{Im}[\beta_o]$ and probabilities scale: Most red = 0.5 and most blue = -0.4.	59
4.9	Wigner function of the states at different time scales under KNR with two-photon drive Hamiltonian. Initial state: even parity cat states $C_{\beta_o}^+$. Here x-axis = $\text{Re}[\beta_o]$ and y-axis = $\text{Im}[\beta_o]$ and probabilities scale: Most red = 0.5 and most blue = -0.4.	59
4.10	Experimental realization of the fp-SQUID integrated over the cavity. Notations of the frequencies are according to the research paper of Grimm et al. [2] but can be changed according to this dissertation.	62

List of Acronyms

QEC	Quantum error correction
QECC	Quantum error correction codes
CQED	Circuit quantum electrodynamics
cQED	cavity quantum electrodynamics
Q.H.O.	Quantum harmonic oscillator
JC	Jaynes Cummings
TLA	Two-level atom
EM	Electromagnetic
RWA	Rotating-wave approximation
FTQC	Fault-tolerant quantum computer
JJ	Josephson junction
SC	Superconducting
PBCs	Periodic boundary conditions
BCs	Boundary conditions
TLR	Transmission line resonators
TLs	Transmission lines
CPB	Cooper pair box
QC	Quantum computing
KNR	Kerr nonlinear resonator
ME	Master equation
WF	Wigner function
SCS	Schrodinger cat states
JPA	Josephson parametric amplifier
2ph-KNR	Two-photon driven Kerr Nonlinear Resonator
CNOT	Controlled NOT

Abstract

Exploiting the non-linearity (Kerr effect) in SC qubits when coupled with microwave resonators showed promising results: thus, creating out-of-phase superpositions of coherent states, commonly called SCS. These cat states are widely used in quantum information processing especially for hardware-efficient quantum computing because of their exponential suppression against bit-flip errors, albeit linear increment in phase-flip errors against the amplitude of the coherent state. However, high-fidelity generation, stabilization, and manipulation (GSM) of these cat states is a challenging task.

In this project, we consider a Kerr nonlinear resonator with an additional two-photon drive and study the evolution of the resonator fock state to cat state using the QuTiP package. We demonstrate that this method can generate stabilized cat states that are robust against single-photon loss. Interestingly, the two-photon drive also cancels the unwanted phase evolution induced by the Kerr effect and dephasing effects due to single-photon loss. Furthermore, we have presented how adiabatic and high-fidelity non-adiabatic initialization of cat states is possible. We found that the cat state preparation using the qcMAP protocol suffers deformation due to self-Kerr effects, but using a two-photon drive can obviate these deformations and thus generate a high-fidelity cat state. Finally, we provided a scheme to realize the quantum logic gates (X gate, Z gate, and Entangling gate) by manipulating those engineered subspaces of KNR. We have also presented a possible experimental realization of KNR with a two-photon drive.

Chapter 1

Introduction

Quantum computing is a fascinating field that exploits the intrinsic properties of quantum mechanics. This concept was initially proposed by Feynman [3] and offers a promising and efficient way to solve intractable problems that classical computers struggle to handle [4, 5]. As a result, many applications have emerged in various fields, including quantum simulation [6], quantum machine learning [7], quantum chemistry [8], and optimization [9]. These applications include factoring [10], which poses a significant threat to RSA encryption. To achieve the potential benefits of quantum computing, we require millions to billions of quantum gates and a quantum processor that must have a low error rate. The error rate of today's quantum processors is around 10^{-3} per gate [11–16] and it becomes much higher when billions of gates are applied to get any useful results e.g. for the applicability of any algorithm like Shor's or Grover which has shown a quantum advantage. Thus, the development of a FTQC is a significant challenge but has

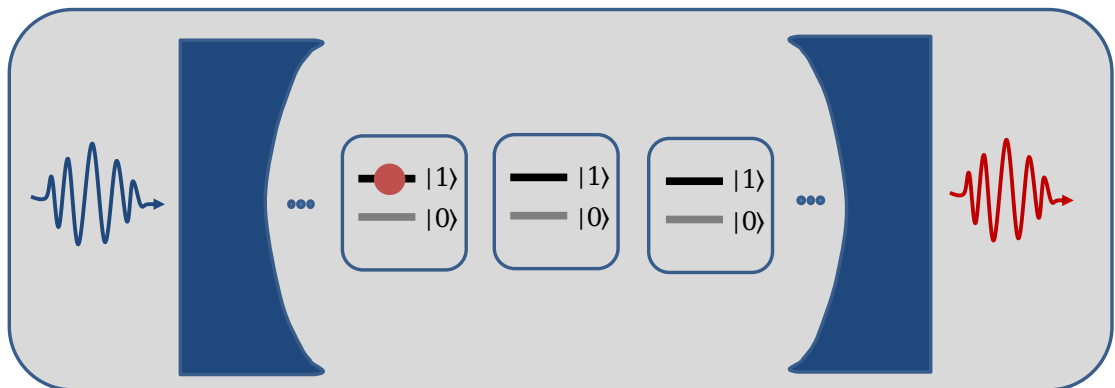


Figure 1.1: Schematics of the general architecture of quantum computing processor containing highly coupled two-level atoms, cavities/resonators, and microwave field.

the potential to revolutionize various sectors [6–9].

Over the past decade, rapid progress has been made in the development of quantum computing technologies [17–26] and the general architecture of any quan-

tum computing processor is shown in Figure 1.1. We are now in the noisy intermediate-scale quantum (NISQ) era [27], with numerous platforms available to encode and process quantum information. These include superconducting qubits [28, 29], trapped ions [30, 31], spin qubits [32, 33], and photons [18, 19, 22], among others. Among these, superconducting qubits have shown great promise for scalable quantum information processing and have become a leading candidate for quantum processors. Their physical properties have gained much attention in recent years, with the number of qubits increasing significantly, and two-qubit operations now being possible [34] with the high-fidelity (approx. 99.4%). Therefore, the global race for quantum supremacy [35] is at its peak, spurred on by recent advances in superconducting quantum systems such as qubit readout [36], and parametric oscillators and amplifiers [37–39]. Moreover, the favorable situation of superconducting microwave resonators which have shown to be very useful for readouts, strong coupling to the qubits, robustness against decoherence [1, 36, 40, 41], and especially improvement in coherence time [42, 43] have made the SC qubit a pertinent choice (due to its integration on SC resonator). Among the three main types of superconducting qubits, the charge-based qubit called Transmon [44, 45] is more robust against noisy electric fields and is now considered a standard qubit. It can be thought of as a nonlinear LC circuit, with the Josephson junction providing the necessary nonlinearity.

The requirement of large-scale quantum computers is to encode information without errors: irreversible processes caused by the interaction of the quantum system with the environment. To address this, various QECC [46] have been developed that encode the quantum information onto energy levels of quantum systems, which helps to detect and correct errors without loss of actual information [47]. The conventional error correction maps the logical states 0 and 1 onto a 2D subspace of Hilbert space that corresponds to concerned states of qubits. However, this method has some limitations, such as a huge hardware footprint and the requirement of strong coupling between physical qubits to achieve quantum advantage. Similarly, we know that when a quantum system is manipulated and measured, it tends to interact with the environment’s degrees of freedom, leading to decoherence albeit we need system/qubit to be coherent while applying gates. However, the quantum information can be non-locally encoded to prevent decoherence as environments are locally correlated. For example, some schemes encode the information in a non-local manner, such as spatial distance [48] or entangled qubit states [49]. The idea of nonlocal encodings is exploited further, and quantum information is encoded to the states that are non-local in the phase space of a harmonic oscillator [50, 51]. This method allows for the detection and correc-

tion of errors while reducing the resource overhead problem ¹. It also improves hardware efficiency by reducing the required physical components and fulfills the requirement of manipulating many strongly coupled physical qubits.

To achieve a FTQC, it must meet several requirements, including a simple physical layout, a high error correction threshold ² that is possible on a large scale, and less resource overhead. While the surface code [55] has a great physical layout, it requires a high resource overhead for any algorithm execution. In other words, all quantum architectures involve trade-offs between the aforementioned objectives. Recent studies [2, 52–54] have shown that qubits with biased noise are the ideal candidate for fault-tolerant quantum computation when implementing noise-preserving gates [56]. The realization of such qubits is through Schrödinger cat states, which can be prepared using different methods, such as two-photon drive or multi-photon dissipation [51, 57]. Two-photon drive [2, 58] exploits the nonlinearity in the Josephson junction element and generates the Schrodinger cat states known as Kerr cat qubits. Multi-photon dissipation happens when cavity field mode is coupled with the bath and the system evolves to cat states commonly called dissipative cat qubits. Other methods, such as the qcMAP protocol [59], use the dispersive interaction between the qubit and cavity. Furthermore, extending Schrödinger cat states to multiple modes, such as entangled coherent states [60], shows a high potential for quantum metrology [61, 62] and for continuous-variable (CV) quantum information [63, 64]. These states can also be prepared experimentally in superconducting circuits using feedback control [65].

Similarly, we have seen that generic QEC is challenging due to two main reasons: the resource overhead problem and threshold requirements. So, to develop QECC, we must consider hardware into account to counter this generalization. For example, making QECC to encounter only excitation loss error which has been experimentally demonstrated in trapped ions [66] and superconducting circuits [67]. Some bosonic codes can suppress errors, such as excitation loss errors, by engineering dissipation (dissipative cat states [51]) or providing a favorable energy gap that gives a biased noise channel (Kerr cat states [58]). Grimm et al., have proved that the coherent state-based QECC can achieve exponential suppression against bit-flip errors [51, 58, 68] against the amplitude of coherent state, albeit linear increase in phase-flip errors against the amplitude of coherent state. Noise bias towards phase-flip errors in cat qubits is caused by an engineered interaction that suppresses the transfer of probabilities between the components of cat

¹ratio of increment in the computer's component vs the protection degree of encoded information provided by QECC

²noise affecting the components of the quantum computer must be below a constant value called the accuracy threshold [52–54]

states, which has also been experimentally demonstrated by Grimm et al. [2]. By providing a highly biased noise channel, these QECC improve resource overhead and error threshold.

Qubit-cavity MAP protocol (qcMAP gate) offers several benefits over other methods of generating Schrodinger cat states. One of the advantages is that it maximizes coherence and requires minimal setup. Additionally, the qubit and cavity frequencies and couplings are fixed. Moreover, the generation time for Schrodinger cat states scales linearly with the number of cat state components, rather than with the amplitude of the cat state itself [59]. This feature allows for the generation of high-amplitude and high-fidelity cat states, which is used to explore the decoherence of nonclassical systems further [69, 70]. The qcMAP gate applies qubit mapping to the cavity state of the cat state, taking advantage of the strong dispersive regime, where the resonator and qubit transition frequencies split into spectral lines [44]. The resonator frequency splits into two well-resolved frequencies, depending on the state of the qubit, such as $\omega_c^g \rightarrow |g\rangle$ and $\omega_c^e \rightarrow |e\rangle$. Similarly, the qubit frequency splits into many frequencies, depending on the number of photons in the cavity. Experimental results show that the dispersive shifts are much larger than the cavity and qubit linewidth [59]. This gate relies mainly on two gates: the conditional displacement operation [71], which displaces the cavity state depending on the qubit state, and the conditional rotation gate [72], which rotates the qubit state depending on the cavity state. The sequence of generating the cat states is as follows: The initial qubit state is taken as a superposition state, and the cavity state is a vacuum state. The first conditional displacement operator is applied to the cavity state by α , and then the given state is evolved through the dispersive Hamiltonian for T_{gate} . After that, the displacement operator is applied again by α . This conditional displacement gate entangles the qubit state with the resonator. Next, the conditional rotation gate (rotation angle = π) is applied to disentangle the given state. Finally, the displacement operator is again applied by $-\alpha$ amplitude to set the superposition state at the center of the phase space.

For the case of multi-photon dissipation method, we know that resonantly driving a damped harmonic oscillator stabilizes the coherent state of the cavity. By engineering the coupling of the environment with the cavity mode field, we can preserve the energy of cat states. The complex amplitude of the coherent state linearly varies with the amplitude of the driving field. By coupling the bath with the harmonic oscillator, energy exchange occurs between them in photon pairs, driving the quantum harmonic oscillator to two-component cat states, C_α^+ and C_α^- , as demonstrated by Wolinsky, Krippner, Hach, Gilles et al. [73–76]. The authors utilized this pair photon-driven dissipative process and determined the asymptotic

behavior of the system and showed that such a process can protect the cat states (logical ground and excited state of the qubit) from photon dephasing channels. However, such an encoded cat qubit is not protected from the single photon loss error channel. To mitigate this error channel, they extended the idea to a four-photon process, in which a four-component cat state becomes a logical basis choice. By utilizing continuous photon number parity measurement [77], they corrected the aforementioned main error channel. Next, applying specific Hamiltonians, the authors presented a toolbox for quantum computation using these cat states [78]. They have proposed possible gate realizations and have shown that these gates are protected from the main decay channels. They have also shown the possible two-photon driven dissipative process and demonstrated that a simple chip-based CQED provides enough flexibility for applying the required Hamiltonians and damping operators for required dissipation. The usefulness of this method is that we require only fixed frequencies and fixed amplitudes. Devices with similar parameters are experimentally shown by Lidar, Kirchmair et al. [79, 80]. However, the realization of four-photon dissipation is still under question. But there is one experimental challenge, to preserve the coherence of the dissipative cat state, that is the rate of two-photon loss must be greater than the single photon loss rate. Moreover, using these states, bias-preserving Toffoli gates, CNOT, and other bias-preserving nontrivial sets of gates have been realized [2, 58, 81, 82].

In this dissertation, we have extensively studied another method [58] to produce the Schrödinger cat states that takes advantage of the Kerr nonlinearity induced by a qubit when placed inside a superconducting resonator with an additional two-photon drive. These states are called Kerr cat states, and their generation can be optimized by careful tuning of the driving strength and frequency. Furthermore, Grimm et al. [2] have shown the experimental implementation of single-qubit operations using these Kerr cat states. They performed all the single-qubit gates with a timescale sixty times faster than coherence time and have shown the single-shot readout of the stabilized qubit. Kang et al. [83] have demonstrated the implementation of nonadiabatic geometric gates using these states and they have realized an occurrence of selective transition of auxiliary qutrit when KNR is coupled with auxiliary qutrit with definite coupling constants. This selective transition is important for the implementation of NOT, phase, controlled phase, and CNOT gates as well the Toffoli gates. Kwon et al. [84] have further strengthened the field by showing the simplest error correction schemes that even surpassed the break-even point³ (using only a single continuous microwave tone and used another microwave tone for the reset schemes).

³critical threshold where the error rates of a quantum system, such as qubits or quantum gates, are kept low enough through error correction techniques

1.1 Thesis Overview

The first chapter is devoted to the literature survey of the exciting field of quantum information processing and quantum computing. The second chapter gives an introduction to the theoretical background and graphical analysis of two-level atoms and the field quantization. It also gives an overview of the representation of quantum states in phase space. Mathematics and analysis of two-level atoms is essential to understand the phenomenon in the physics of qubits. Similarly, following the mathematics of chapter two, the third chapter is an introduction to circuit quantum electrodynamics. This chapter extensively provides the details of the Hamiltonians of various systems like transmission lines, resonators, Josephson junctions, and qubits. This chapter also entails the processes in the quantum physics of qubit interaction with the field and the environment. The fourth chapter is all about how to stabilize and manipulate the Kerr cat states generated by exploiting the non-linearity (Kerr effect) in SC resonators i.e. microwave resonators. It describes the methods we followed and the analysis of the results, and the discussion.

Chapter 2

Two-level System and Field Quantization

The two-level system serves as a fundamental concept in the exploration of quantum mechanics. This physical framework allows for the consideration of the excited, ground, or superposition of both states of an atom. In order to provide a mathematical framework for the two-level system, a 2D Hilbert space is employed. Many systems within quantum mechanics can be effectively approximated as two-level systems, and the study of their interaction with the quantized EM field adds further intrigue to the field of physics. Consequently, this chapter is dedicated to delve into the mechanics underlying the two-level system and its interaction with the laser field. Quantum systems can exist in various states, such as Fock states or coherent states, which are thoroughly elucidated in the concluding sections of this chapter.

2.1 Two Level Systems

The state of an arbitrary two-level system is represented by 2D Hilbert space as follows: $|\psi\rangle = c_g |g\rangle + c_e |e\rangle$. For the state function to be normalized: $|c_g|^2 + |c_e|^2 = 1$, where c_g and c_e are the probability amplitudes of the atom to be found in the ground and excited state, respectively. Generally, the Hamiltonian of a two-level system is written in terms of Pauli matrices as follows:

$$\hat{H} = \bar{\epsilon} \cdot \bar{\sigma} = \bar{\epsilon}_x \cdot \bar{\sigma}_x + \bar{\epsilon}_y \cdot \bar{\sigma}_y + \bar{\epsilon}_z \cdot \bar{\sigma}_z, \quad (2.1)$$

where $\bar{\epsilon} = (\bar{\epsilon}_x, \bar{\epsilon}_y, \bar{\epsilon}_z)$ are the eigenvalues or coupling terms between energy levels, and $\bar{\sigma} = (\bar{\sigma}_x, \bar{\sigma}_y, \bar{\sigma}_z)$. The dynamics of the system is explained by the evolution of the Hamiltonian of the system in time. As Hamiltonian contains the Pauli

matrices/operators and we know that operator dynamics is represented by the Heisenberg picture following the Heisenberg equation of motion as:

$$\frac{d}{dt}\hat{A}(t) = \frac{1}{i\hbar}[\hat{A}(t), \hat{H}] + \frac{\partial}{\partial t}\hat{A}(t). \quad (2.2)$$

We can write the Heisenberg equation of motion of Pauli matrices which are not explicitly dependent on time, aforementioned in the Hamiltonian of the general two-level atom, as follows:

$$\frac{d\sigma_x}{dt} = \frac{2}{\hbar}(\vec{\epsilon} \times \hat{\sigma})_x. \quad (2.3)$$

Similarly, $\frac{d\sigma_y}{dt} = \frac{2}{\hbar}(\vec{\epsilon} \times \hat{\sigma})_y$ and $\frac{d\sigma_z}{dt} = \frac{2}{\hbar}(\vec{\epsilon} \times \hat{\sigma})_z$ completely describes the evolution of Pauli matrices. These equations are analogous to classical gyroscope dynamics. Following this analogy, we can say that Pauli vectors ($\hat{\sigma}$) precesses around $\vec{\epsilon}$ with angular frequency $|\frac{2\vec{\epsilon}}{\hbar}|$. The expectation value of the operator gives the notion of a Bloch vector if it is graphically visualized. Here, we consider a general two-level system with the following Hamiltonian:

$$H = \begin{pmatrix} E_z & E_x \\ E_x & -E_z \end{pmatrix}. \quad (2.4)$$

We diagonalize \hat{H} and get subsequent eigenvalues: $E = \pm\sqrt{E_x^2 + E_z^2}$. We set E_x fixed and check out the behavior of E vs E_z where E_z is a controllable parameter. The Fig. 2.1 consists of two linear lines intersecting at a point called the degeneracy point A . This occurs when $E_x = 0$, indicating that the system is in a degenerate state where both energy levels have the same energy. When E_x is turned on, an avoided crossing is observed in the figure. An avoided crossing indicates that the energy levels repel each other as E_z varies. As a result, two distinct energy branches emerge from the degeneracy point A . The avoided crossing suggests that there are two distinct states in the system, P and Q, corresponding to the two branches. These states have different energy values and are the superposition of the original basis states. This behavior is a characteristic feature of a two-level system in the presence of a controllable parameter, where the system's energy levels undergo non-trivial changes as the parameter is varied.

Next, we consider the TLA interacting with the classical EM field (semi-classical approach). The semi-classical approach can correctly predict the behavior of transitions of probabilities in the two-level systems but it has some limitations like this approach cannot explain some phenomena occurring in nature e.g. spontaneous emission. Considering that the Laser field is given by: $\bar{E} = \hat{\eta}E_o \cos(\omega t)$, here $\hat{\eta}$ is the polarization direction and E_o is the amplitude of the field with the frequency ω . We have considered here two approximations: 1. Wavelength of

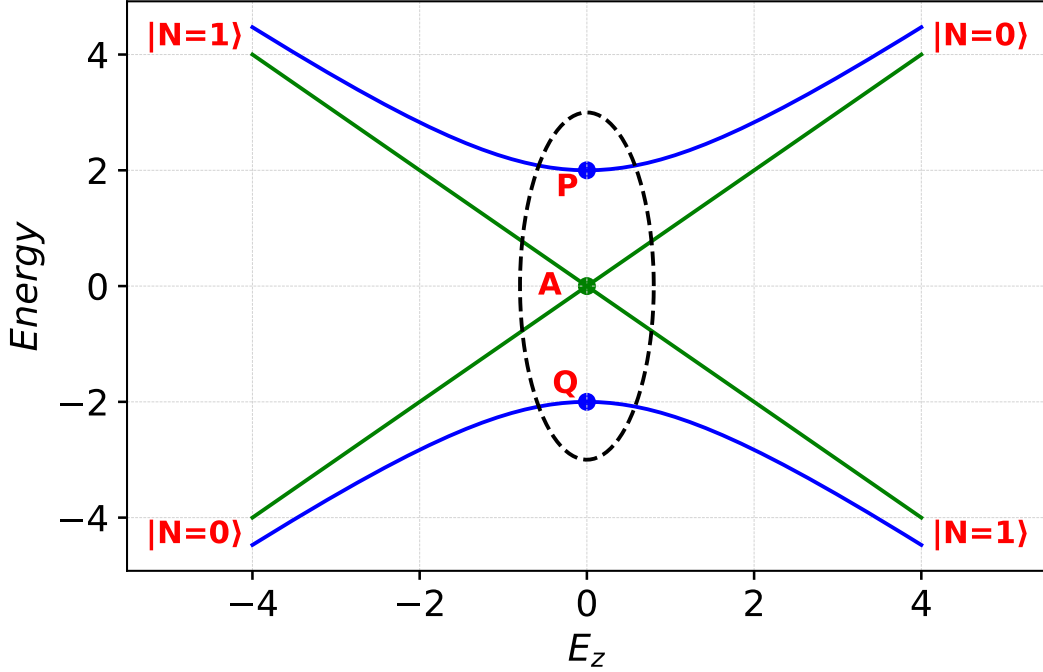


Figure 2.1: Plot of E vs E_z when $E_x = 0$ (green curve) and $E_x \neq 0$ (blue curve). For the case when $E_x \neq 0$ then we get a superposition of basis states $P = \frac{1}{\sqrt{2}} \begin{pmatrix} 1 \\ 1 \end{pmatrix}$ and $Q = \frac{1}{\sqrt{2}} \begin{pmatrix} 1 \\ -1 \end{pmatrix}$

the laser is larger than the size of the atom i.e. dipole approximation, thus we ignore the variation of the field over the atom. 2. We have not considered the spatial dependence of the field. Expanding the *cosine* term in electric field expression, we can write it as $E(t) = E^+(t) + E^-(t)$ having $E^+(t) = \exp\{-i\omega t\}$ and $E^-(t) = \exp\{i\omega t\}$. The Hamiltonian of the system consisting of the two-level atom and classical EM field is given by:

$$H = H_A + H_{AF}, \quad (2.5)$$

where H_A describes the Hamiltonian of TLA and H_{AF} delineates the interaction of atom with EM field. Writing the Hamiltonian of atom in the basis $|g\rangle$ and $|e\rangle$, we have $H_A = \hbar\omega_g |g\rangle\langle g| + \hbar\omega_e |e\rangle\langle e|$ and $H_{AF} = \hat{\mu} \cdot \vec{E}$. Here $\hat{\mu} = -e \cdot \vec{r}_e$ is the dipole moment of the electron. Similarly, to pen down the dipole moment in the given basis, we have dipole matrix elements as follows: $\hat{\mu} = \langle g | \mu | e \rangle (|g\rangle\langle e| + |e\rangle\langle g|)$. Transforming the given Hamiltonian in terms of atomic lowering and raising operator $\sigma = |g\rangle\langle e|$ and $\sigma^\dagger = |e\rangle\langle g|$ respectively and hence, given moment operator looks like:

$$\hat{\mu} = \langle g | \mu | e \rangle (\sigma + \sigma^\dagger). \quad (2.6)$$

We also apply RWA, ignoring the fast oscillating terms and considering only slowly

varying terms because we are interested near detuning $\Delta = \omega_e - \omega_g$, we write the atom-field Hamiltonian as follows:

$$H_{AF} = \frac{\hbar\Omega}{2}(\sigma \exp\{i\omega t\} + \sigma^\dagger \exp\{-i\omega t\}), \quad (2.7)$$

where $\Omega = -\frac{\langle g|\hat{r}\cdot\vec{\mu}|e\rangle}{\hbar}E_o$ characterizes the strength of atom-field coupling and is commonly called Rabi frequency. Assuming the atom is prepared in the superposition state $|\psi\rangle = c_g|g\rangle + c_e|e\rangle$ and finding out the dynamics of the two-level atom by applying the Schrodinger equation for its evolution over time $i\hbar\frac{\partial|\psi\rangle}{\partial t} = (H_A + H_{AF})|\psi\rangle$. After plugging the required expressions, we get the following coupled differential equations of the coefficients (whose squares are respective probabilities for the atom to be found in the ground or excited state):

$$\frac{\partial c_g}{\partial t} = -i\frac{\Omega}{\exp\{i\omega t\}}c_e, \quad \frac{\partial c_e}{\partial t} = -i\omega_o c_e - i\frac{\Omega}{\exp\{-i\omega t\}}c_g. \quad (2.8)$$

To simplify the calculations, we remove the explicit time dependence in the coupled differential equations. For that applying the co-rotating frames $\tilde{c}_e = c_e \exp\{i\omega t\}$ and $\tilde{c}_g = c_g$ and the transformed Hamiltonian is:

$$H = \begin{pmatrix} 0 & \frac{\hbar\Omega}{2} \\ \frac{\hbar\Omega}{2} & \hbar\Delta \end{pmatrix}. \quad (2.9)$$

Let's first assume the resonant case $\omega = \omega_o$ such that $\Delta = 0$, we obtain uncoupled differential equations. By solving these equations with the initial conditions at $t = 0 \rightarrow c_g(0) = 1$ and $\tilde{c}_e(0) = 0$, we have the following solutions to the coefficients and consequently the respective probabilities of the vector state.

$$c_g(t) = \cos\left(\frac{\Omega}{2}t\right) \quad P_g(t) = \frac{1}{2}(1 + \cos(\Omega t)) \quad (2.10)$$

$$c_e(t) = -i \sin\left(\frac{\Omega}{2}t\right) \quad P_e(t) = \frac{1}{2}(1 - \cos(\Omega t)) \quad (2.11)$$

Plotting the probabilities versus Rabi frequency gives rise to population oscillations, a phenomenon called Rabi flopping. The graph is given below in Figure 2.2 which delineates the concept that probabilities are transferred from the ground state to the excited state and vice versa.

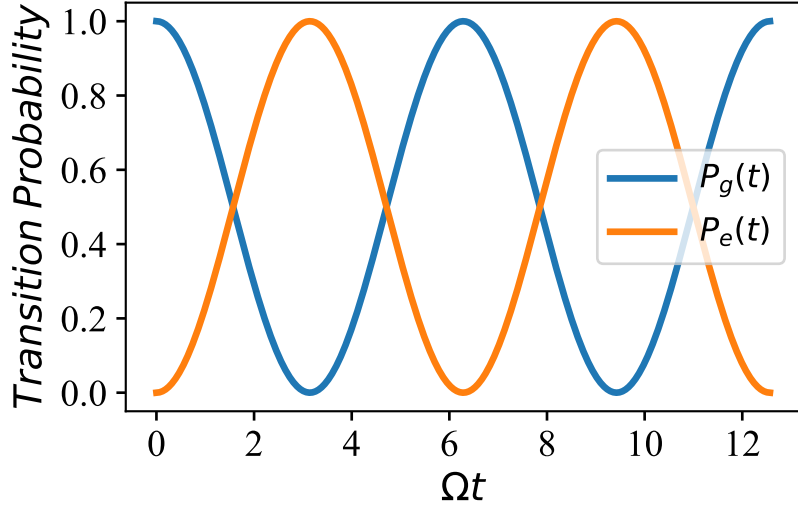


Figure 2.2: Rabi flopping: transfer of probabilities from both states happening with a period of $\Omega t = \pi$. $P_g(t)$ (blue) describes the probability of a state being found in the ground state and $P_e(t)$ (orange) describes the excited state probability.

Next, we consider an off-resonant case such that $\Delta \neq 0$ to see the dynamics of the two-level atom. The uncoupled differential equations are solved by taking out the same strategy of changing the frame to a co-rotating frame and applying RWA with the initial conditions as follows $c_g(0) = 1$ and $c_e(0) = 0$, we get the final form as:

$$c_g(t) = \exp\left\{\frac{i\Delta t}{2}\right\} \left[\cos\left(\frac{\tilde{\Omega}t}{2}\right) - \frac{i\Delta}{\tilde{\Omega}} \sin\left(\frac{\tilde{\Omega}t}{2}\right) \right], \quad (2.12)$$

$$c_e(t) = -i \exp\left\{\frac{i\Delta t}{2}\right\} \frac{\Omega}{\tilde{\Omega}} \sin\left(\frac{\tilde{\Omega}t}{2}\right), \quad (2.13)$$

here, $\tilde{\Omega} = \sqrt{\Omega^2 + \Delta^2}$ is the generalized Rabi frequency. So, the excited state population will be as $P_e(t) = \frac{\Omega^2}{\tilde{\Omega}^2} \sin^2\left(\frac{\tilde{\Omega}t}{2}\right)$ which is plotted in Fig. 2.3. We can see from the plot that the transfer of population never reaches to 1 when we include the factor of detuning and for weak fields $|\Delta| \gg \Omega$ the generalized Rabi frequency is almost equal to detuning and correspondingly for strong fields i.e. $|\Delta| \ll \Omega$, generalized Rabi frequency is almost equal with the Rabi frequency Ω .

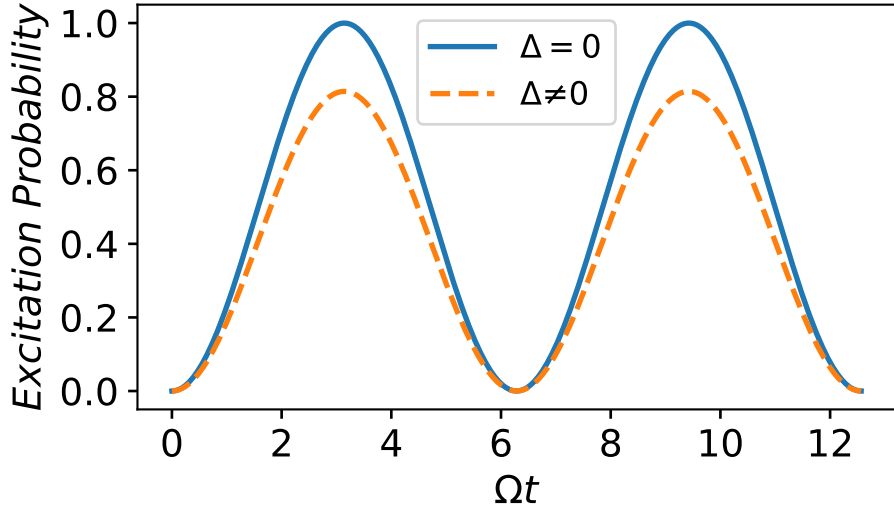


Figure 2.3: $P_e(t)$ (blue line) is the probability of TLA to be found in the excited state when detuning is zero while $P_e(t)$ (orange line) is the excited state probability as a function of Rabi frequency when there is a factor of detuning.

2.2 Classical to Quantum Regime

To quantize any system i.e. from a classical picture to a quantum mechanical picture, there are many methodologies that are followed. The following methodology is one of them and it is named after Dirac, and given as:

- Find Lagrangian of the system $L(q_i, \dot{q}_i)$ of the classical system.
- Find the Hamiltonian $H(q_i, p_i) = \sum p_i \dot{q}_i - L(q_i, \dot{q}_i)$ by Legendre transformation.
- Check the Poisson bracket relation for two conjugate variables: $\{q_i, p_i\} = \delta_{ij}$
- Look for appropriate conjugate variables which follow Hamilton's canonical equations of motion: $\dot{q}_i = \frac{\partial H}{\partial p_i}$ and $\dot{p}_i = -\frac{\partial H}{\partial q_i}$.
- Make the following transformations from the classical to the quantum regime.

$$\begin{array}{ccc}
 H & \longrightarrow & \hat{H} \\
 \{q_i, p_i\} = \delta_{ij} & \longrightarrow & [q_i, p_i] = i\hbar \\
 q_i \text{ and } p_i & \longrightarrow & \hat{q}_i \text{ and } \hat{p}_i
 \end{array}.$$

2.2.1 Quantum Harmonic Oscillator

Harmonic oscillators describe the dynamics of the system close to an equilibrium state. Every system is approximated as a harmonic system if it is perturbed a

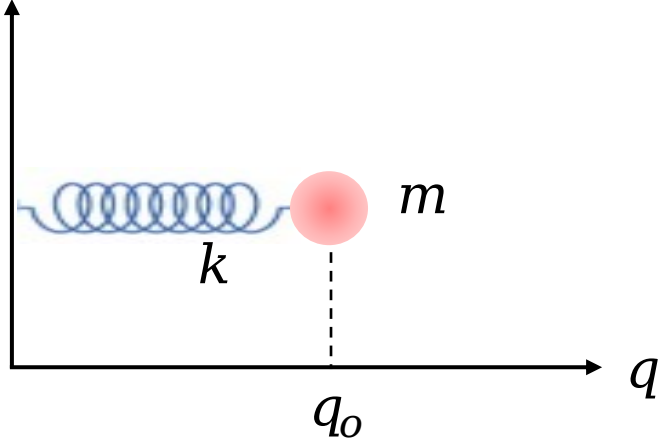


Figure 2.4: Schematic of *mass – spring* system with a spring constant k having frequency $k = \sqrt{m\omega^2}$. Mass m is oscillating around equilibrium position q_o .

little bit around its stable equilibrium point. Spring-mass system is a widely used example to simulate the dynamics of the harmonic oscillator which has quadratic potential term. To quantize a harmonic oscillator (see Figure 2.4), we follow the above *Dirac criteria* for the transformation. As we know that the lagrangian $L(q, \dot{q})$ of the system is given as:

$$L = \frac{1}{2}m\dot{q} - \frac{1}{2}m\omega^2q^2. \quad (2.14)$$

By utilizing Legendre's transformation to connect the Lagrangian and Hamiltonian formulations, we can derive the Hamiltonian as $H = \dot{q}p - L$. By substituting the expression for the Lagrangian into this equation, we obtain the transformed representation of the Hamiltonian as:

$$H = \frac{p^2}{2m} + \frac{1}{2}m\omega^2q^2. \quad (2.15)$$

As any pair of variables can be canonically conjugate variables if they satisfy Hamilton's equations of motion: $\dot{q} = \frac{\partial H}{\partial p}$ and $\dot{p} = -\frac{\partial H}{\partial q}$. These variables also follow the Poisson bracket relation: $\{q, p\} = 1$. We transform the variables into operators as the required conditions are fulfilled. Finally, the Hamiltonian of the Q.H.O. becomes as:

$$\hat{H} = \frac{\hat{p}^2}{2m} + \frac{1}{2}m\omega^2\hat{q}^2. \quad (2.16)$$

Making a substitution as the sum of canonically conjugate variables and setting it equal to lowering operator as $\hat{a} = \frac{1}{2q_o}(\hat{q} + \frac{i\hat{p}}{m\omega})$ and applying the Schrodinger equation: $\hat{H}|\psi\rangle = E_n|\psi\rangle$, we obtain the energy levels as follows:

$$E_n = \hbar\omega(n + \frac{1}{2}), \quad (2.17)$$

where $\hat{N} = \hat{a}^\dagger \hat{a}$ is the number operator and its eigenvalue $n = 0, 1, 2, 3, \dots$ describes the number of level/excitation. $n = 0$ describes the energy at the ground state which is commonly called vacuum energy. One thing that is noticeable is that the Q.H.O. has a constant energy difference between the levels as shown in Figure 2.5.

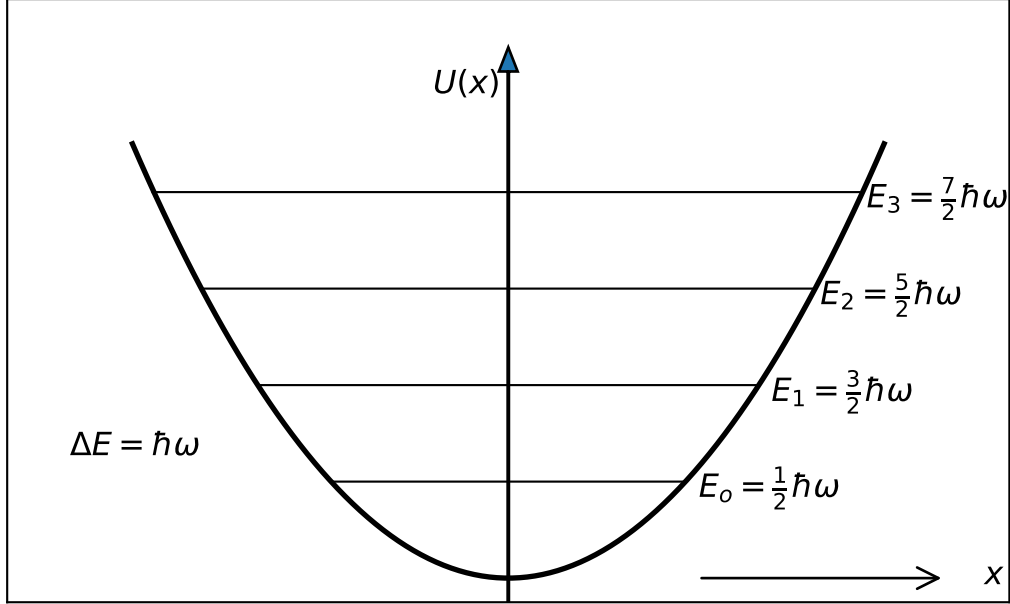


Figure 2.5: Plot of the quadratic potential $U(x)$ of Q.H.O. and energy levels of the Q.H.O. having a constant energy level difference $\Delta E = E_n - E_{n-1}$

Following the same strategy, we derive the Hamiltonian of coupled two harmonic oscillators with an effective spring constant k as follows:

$$\hat{H} = \hbar\omega_1(\hat{a}_1^\dagger \hat{a}_1) + \hbar\omega_2 \hat{a}_2^\dagger \hat{a}_2 - kq_1 q_2 (\hat{a}_1 + \hat{a}_1^\dagger)(\hat{a}_2 + \hat{a}_2^\dagger), \quad (2.18)$$

where $q_1 = \sqrt{\frac{\hbar}{2m\omega_1}}$ and $q_2 = \sqrt{\frac{\hbar}{2m\omega_2}}$ are the zero point fluctuations of the first and second oscillator, respectively. The first term in the Hamiltonian corresponds to the first oscillator, while the second term corresponds to the second oscillator. The third term represents the interaction between these two oscillators, wherein an effective spring constant, denoted as k , governs their coupling. To simplify the analysis and focus solely on the interaction between the oscillators, we expand the third term while neglecting the other two terms i.e. $\hat{a}_1 \hat{a}_2$ and $\hat{a}_1^\dagger \hat{a}_2^\dagger$. These terms in the product expansion only contribute to the overall energy spectrum scaling and do not actively participate in the system's dynamics. Consequently, by applying the RWA, we derive the final form of the Hamiltonian as follows:

$$\hat{H} = \hbar\omega_1(\hat{a}_1^\dagger \hat{a}_1) + \hbar\omega_2 \hat{a}_2^\dagger \hat{a}_2 - hg(\hat{a}_1^\dagger \hat{a}_2 + \hat{a}_1 \hat{a}_2^\dagger). \quad (2.19)$$

Here, $g = \frac{kq_1q_2}{\hbar}$ is the coupling coefficient between two quantum harmonic oscillators.

2.3 Quantization of Electromagnetic Waves

Maxwell's equations fulfill a pivotal role in the investigation of electromagnetic radiation. Within the framework of quantum theory, electromagnetic radiation can be quantized into discrete energy packets known as photons. The electromagnetic field comprises two vector fields: the electric field and the magnetic field.

In the next section, we will see how to quantize these fields and how useful it is, by treating them as Q.H.O. in a state of equilibrium.

2.3.1 Deriving the Hamiltonian of traveling EM Waves

The energy of an EM field in a given mode is given by:

$$H = \frac{\epsilon_o}{2} \int \bar{E}^2 + c^2 \bar{B}^2 d^3r, \quad (2.20)$$

ϵ_o is the permittivity of free space and \bar{E} and \bar{B} are the electric and magnetic field amplitudes, respectively. For travelling waves $\bar{E} = c^2 \bar{B}^2$, now let $E = \hat{x}E_o(t)e^{iky} + c.c.$ ¹ where electric field amplitude is $E_o(t) = |E_o(t)|e^{i\phi}$ with a phase factor ϕ and \hat{x} is the polarization vector. The electric field is written in the full description as follows:

$$\bar{E} = \hat{x}2|E_o(t)| \cos(ky + \phi). \quad (2.21)$$

Traveling waves follow certain PBCs: $\bar{E}(y = 0) = \bar{E}(y = l)$, so by applying the given PBCs, we get the quantized frequency $\omega_m = \frac{m\pi c}{L}$ through the periodicity condition $e^{iky} = 1$. Assuming $\phi = 0$ and plug it into the above Hamiltonian and solve for the volume of the box as follows:

$$H = \epsilon_o \int_0^L \int_0^L \int_0^L 4|E_o(t)|^2 \cos^2(ky) dx dy dz. \quad (2.22)$$

Plugging here wave vector $k = \frac{m\pi}{L}$ and $E_o(t) = iA\alpha(t)$, where A having the dimension of electric field and α is a dimensionless parameter. This expression $\frac{\partial \alpha}{\partial t} = -i\omega\alpha(t)$ fully describes the dynamics of the electric field in a single mode by taking its analogy with the dynamics of EM field propagating along $+k$ direction which is described by $\frac{\partial E_o}{\partial t} = -i\omega E_o$. Thus, after integration of the aforementioned

¹c.c. stands for its complex conjugate part

H , we get the following equation:

$$H = 2\epsilon_o A^2 V |\alpha(t)|^2, \quad (2.23)$$

where $A = \sqrt{\frac{\hbar\omega}{2\epsilon_o V}}$, V is a quantization volume, a volume whose boundary conditions are given above, and A is the amplitude of field that has energy $\hbar\omega$ in the volume of quantization. Now defining $\alpha(t) = \frac{1}{2\hbar}(q + ip)$ as q and p are canonically conjugate variables, we will get the Hamiltonian as follows:

$$H = \frac{\omega}{2}(q^2 + p^2). \quad (2.24)$$

By employing the so-called *Dirac criteria* for quantization, we shall proceed with the prescribed procedure to derive the final expression for the quantized Hamiltonian.

$$\hat{H} = \hbar\omega(a^\dagger a + \frac{1}{2}). \quad (2.25)$$

Here, $\hat{a}^\dagger \hat{a}$ is the number operator and gives the depiction of the number of excitation/quanta in the quantum harmonic oscillator. We note from the quantized Hamiltonian that the modes of EM field oscillate like a harmonic oscillator. Similarly, for infinite modes, we sum over modes and the corresponding energy is $E = \sum_{\lambda} \hbar\omega(n_{\lambda} + \frac{1}{2})$ where for λ mode $|n_{\lambda}\rangle$ is the number of photons/excitations. The electric and magnetic fields are given by:

$$\hat{E} = i\sqrt{\frac{\hbar\omega}{2\epsilon_o V}}\bar{\eta}[\hat{a}e^{ik\cdot r} - \hat{a}^\dagger e^{-ik\cdot r}], \quad (2.26)$$

and

$$\hat{B} = i\sqrt{\frac{\hbar}{2\epsilon_o V\omega}}(\bar{k} \times \bar{\eta})[\hat{a}e^{ik\cdot r} - \hat{a}^\dagger e^{-ik\cdot r}]. \quad (2.27)$$

2.3.2 Model the Hamiltonian of stationary EM Waves

Standing waves are produced by the combination of two waves traveling in opposite directions with identical frequency and amplitude. This interaction leads to constructive and destructive interference, resulting in a stationary wave pattern. Unlike traveling waves that propagate through space, standing waves do not exhibit forward movement. Instead, they appear to be fixed or "standing" in a particular area. Nodes, which are points of minimal or zero amplitude, and antinodes, which are points of maximum amplitude, are characteristic features of standing waves. These points remain stationary in space. Standing electromagnetic waves can form in systems with boundaries or resonant structures that allow for the reflection of waves back and forth. Familiar examples of standing waves

are observed in microwave resonators or transmission lines. Within these systems, specific frequencies can trigger resonance, causing the formation of distinct stationary patterns. The accompanying Figure 2.6 provides a representation of a

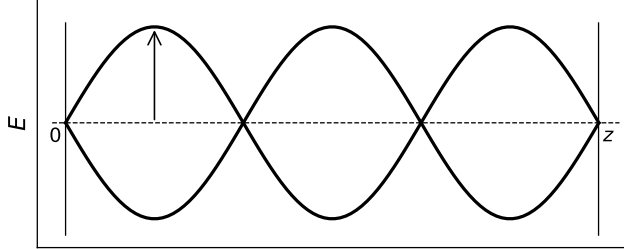


Figure 2.6: Representation of the standing wave mode of the electric field with the two plane mirrors placed at 0 and z .

distinct mode of a standing wave, considering the specified boundary conditions spanning from 0 to z . However, for the purpose of our analysis, we focus solely on a particular mode of the standing wave. Consequently, the full mathematical description of the standing EM wave is given as:

$$\bar{A}(z, t) = \bar{\eta}A(t) \sin(kz), \quad \bar{E}(z, t) = \bar{\eta}E(t) \sin(kz), \quad \bar{B}(z, t) = (\bar{k} \times \bar{\eta})A(t) \cos(kz). \quad (2.28)$$

Here, $\bar{A}(z, t)$ is the vector potential along the z -direction with the polarization direction along $\bar{\eta}$. $\bar{E}(z, t)$ and $\bar{B}(z, t)$ are the electric and magnetic field components of the EM standing wave. From the boundary conditions: $\bar{E}(0, t) = \bar{E}(L, t) = 0$, we get discretized wave vector from the given BCs as $k_n = n\frac{\pi}{L}$. Using the expression of the energy of mode as written earlier and plugging the expressions for fields and potential, we get the final form of Hamiltonian as follows:

$$H = \epsilon_o N^2 V |\alpha|^2, \quad (2.29)$$

where the dimensionless variable $\alpha = \frac{1}{2N}(\omega A - iE)$, normalizing factor $N = \sqrt{\frac{\hbar\omega}{\epsilon_o V}}$ and V is the quantization volume. There is a factor of ‘2’ in the normalization constant of traveling waves and is not present in the standing wave case because of the uniform distribution of energy in the traveling wave case. Defining the conjugate pairs $q = \sqrt{\frac{\epsilon_o V \omega}{2}} A(t)$ and $p = \sqrt{\frac{\epsilon_o V}{2\omega}} E(t)$ and following the *Dirac criteria* for quantization and making some type of substitutions, we get observables in final form as follows:

$$\hat{A}(z, t) = \bar{\eta} \frac{1}{\omega} \sqrt{\frac{\hbar\omega}{\epsilon_o V}} (\hat{b} + \hat{b}^\dagger) \sin(kz). \quad (2.30)$$

Similarly, the other conjugate pair is given as:

$$\hat{E}(z, t) = i\bar{\eta} \frac{1}{\omega} \sqrt{\frac{\hbar\omega}{\epsilon V}} (\hat{b} - \hat{b}^\dagger) \sin(kz). \quad (2.31)$$

Making the comparison of the wave modes of the traveling and standing waves, both wave modes behave like a Q.H.O. when quantized but there are differences: The traveling wave mode has definite energy and momentum while the standing wave doesn't have definite momentum but it has a definite average energy.

2.4 Quantum States and its Representation

The quantum states of a Q.H.O. are classified into different types based on their characteristics. Here are some of the states that are used in this dissertation. i.e. Fock states, coherent states. Fock states, represented by $|n\rangle$, are widely used

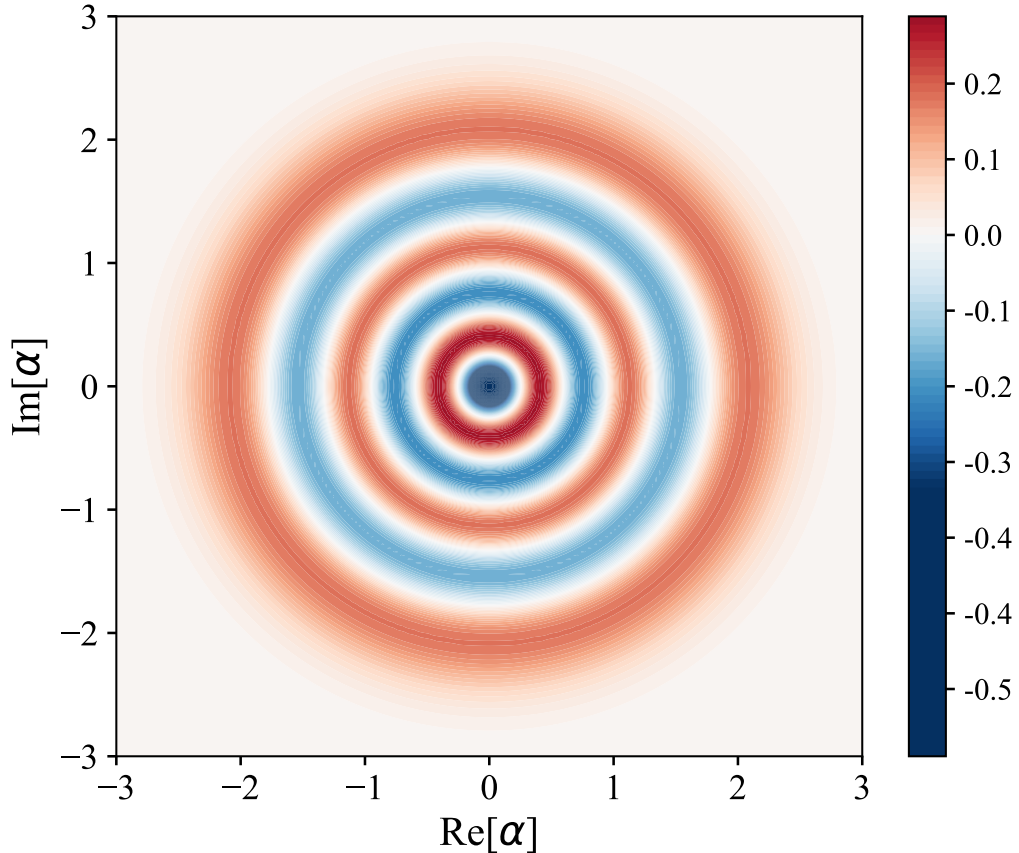


Figure 2.7: Wigner function of the fock state of a harmonic oscillator whose level number 5 is excited. Negative probabilities are the depiction that the state is a quantum state. $Re[\alpha]$ and $Im[\alpha]$ are the corresponding canonically conjugate pairs.

states in the context of Q.H.O. It is like we take the number of photons/quanta

as a basis for the representation of the state of the system. This state is also called number state i.e. being the eigenstate of the number operator of Q.H.O., and it tells us the number of excitation. The wavefunction of the fock state is the product of the Hermite polynomial and Gaussian function. The projection of quadrature operator \hat{X} with the state function of the harmonic oscillator gives the probability of finding the oscillator in the state with quanta n :

$$P^{(0)}(X_1) = |\langle X_1 | 0 \rangle|^2 = \sqrt{\frac{2}{\pi}} \exp(-2X_1^2) \frac{1}{2^n n!} \left(H_n(\sqrt{2}X_1) \right)^2, \quad (2.32)$$

with the fluctuation in one of the quadrature as $\Delta X_1 = \frac{1}{2}\sqrt{2n+1}$. Fock states are used as a basis for the representation of the quantum state, and the for the calculation of the transition probabilities. They are represented using the Wigner function, classical phase space analog, consisting of the quadrature operators as \hat{x} and \hat{p} . Wigner functions are the quasi-probability distribution function because of getting negative probabilities which are the depiction of the quantum nature. Figure 2.7 shows the probability distribution/Wigner function for the fock state of the harmonic oscillator with an excitation energy level, $n = 5$ [85]. Similarly, the vacuum state is the ground state of Q.H.O. and it is a fock state with a fluctuation in each of the quadratures = 1/2. The probability distribution is given as:

$$P^{(0)}(X_1) = |\langle X_1 | 0 \rangle|^2 = \sqrt{\frac{2}{\pi}} e^{-2X_1^2} \quad P^{(0)}(X_2) = |\langle X_2 | 0 \rangle|^2 = \sqrt{\frac{2}{\pi}} e^{-2X_2^2}. \quad (2.33)$$

The vacuum state is the minimum possible energy state with the uncertainty relation $\Delta X_1 = \sqrt{\langle 0 | X_1^2 | 0 \rangle - \langle 0 | X_1 | 0 \rangle^2} = \frac{1}{2}$. And it has many interesting applications in the study of the foundations of quantum mechanics and even in the industry i.e. quantum cryptography. The vacuum field in analogy with the classical field ² is that the field quadrature operator fluctuates and the mean value of them corresponds to zero as is validated through a given figure 2.8. For a coherent state, the uncertainty relation between the average value of position and momentum is exactly equal to the Heisenberg uncertainty threshold, minimum uncertainty, which comes out of the commutation relation. They are also known as Glauber states after the theoretical prediction of physicist Glauber. They are widely used in quantum optics experiments. The coherent state is also the displaced form of the vacuum state in the Wigner function. Coherent states are represented by $|\alpha\rangle = D(\alpha)|0\rangle$ and these states are represented in terms of the

²By classical, it means in phasor diagram

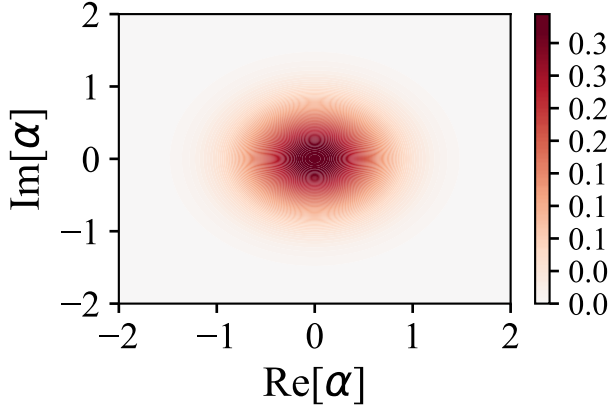


Figure 2.8: Wigner function of vacuum state of the quantum harmonic oscillator.

superposition of fock basis:

$$|\alpha\rangle = e^{-|\alpha|^2} \sum_{n=0}^{\infty} \frac{\alpha^n}{\sqrt{n!}} |n\rangle. \quad (2.34)$$

The coherent states are quasi-orthogonal states and for large amplitude α , they become quite orthogonal states. The amplitude of the coherent states determines how far the given state is displaced from the origin of the Wigner function (mean value of the vacuum state). The coherent state follows the Poisson distribution.

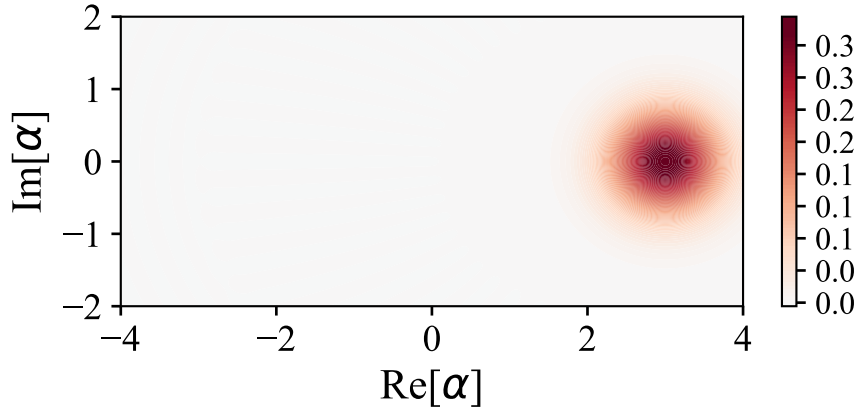


Figure 2.9: Wigner function of coherent state with the amplitude $\alpha = 3$ (real quantity but it can be an imaginary number)

Chapter 3

Circuit Quantum Electrodynamics

Starting with the basic question what is QED? The interaction of atoms with light at the quantum level stands as quantum electrodynamics (QED). There are many processes happening around us just because of the quantumness of the systems: the atom gets coupled with the vacuum fluctuations resulting in spontaneous decay, the splitting of energy levels shown below schematically in Figure 3.1, and Lamb shift due to which degeneracy of the energy levels get lifted, etc. Cavity QED (cQED) is the trapping of the field mode inside the cavity shown below by a cartoon Figure 3.2. Circuit QED (CQED) is analogous to cQED but here the EM radiation gets trapped inside different circuits. Mostly in CQED, we study the behavior of electrical circuits that operate at microwave frequencies.

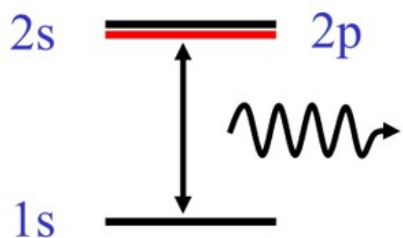


Figure 3.1: Schematic of the Lamb shift lifting the degeneracy between 2s and 2p and emitting a quantum of light.

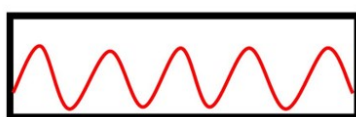


Figure 3.2: Schematic of the field mode being trapped inside the cavity.

3.1 Superconductivity and Cooper Pair Box

Superconductivity is the complete disappearance of electrical resistance in some solids when they are cooled below the critical temperature (T_c). Heike Kamerlingh Onnes discovered Superconductors in 1911 and was awarded Nobel Prize in 1913. He studied that the Mercury wire becomes a superconductor at a critical temperature $T_c = 4K$. He also concluded that any superconductor can return to non-superconducting material by passing a large current through the material or applying a sufficient magnetic field to it. After then, the BCS theory was put forward by Bardeen, Cooper, and Schindler in 1957, and awarded Nobel Prize in 1972. BCS theory states that other than the coulomb repulsion between $2e^-s$, there is a tendency towards attraction between two electrons due to the presence of phonons (quanta of vibrations). Due to phonons, two electrons are glued to each other, forming a cooper pair. In normal metals, spacing between the energy levels depends upon the size of the metallic island. But in superconductors, the energy 2Δ (required for the breakdown of the cooper pair) does not depend on the size of the SC island. BCS theory successfully predicted the value of 2Δ and T_c , and gave a relation between 2Δ and T_c as follows:

$$2\Delta(T = 0) = \frac{7}{2}k_B T_c. \quad (3.1)$$

Here, k_B and T_c are the Boltzmann's constant and critical temperature of the superconducting material, respectively. In the normal metal island, due to many interactions happening at every energy level, energy levels show a continuum of values but in a superconductor, the energy levels show a gap of 2Δ in the energy states. The main reason is that the cooper pairs are bosons and at low temperature, they occupy the same ground state. So, to have two energy levels allowing the system to exhibit two degrees of freedom, we use two SC islands with an insulated gap between them. Cooper pair tunnels from one island to another. This is called a **cooper pair box (CPB)**. The circuit diagram of the CPB is shown in Fig. 3.3.

Considering two SC islands that have two degrees of freedom for the transfer of cooper pairs, these two islands are modeled as the capacitor. In general, the CPB consists of two SC islands (Al) and an insulator inside them (Al_2O_3) with a typical dimension of few μm . When one cooper pair tunnels from one island to another, the remaining charge distribution becomes smooth on each island. The upper island is deficient of one cooper pair while the lower is in excess of one cooper pair charge. Thus, it creates a potential difference that stores an electric field inside them and is modeled as a capacitor. The charge on the islands is exactly similar

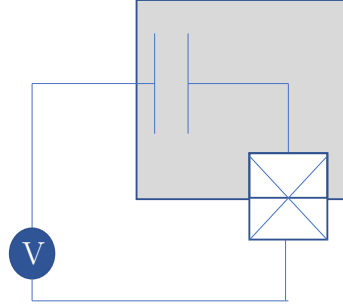


Figure 3.3: Circuit diagram of charge qubit containing a Josephson junction (JJ) and is coupled through an externally applied voltage. One part of the shunted capacitor and JJ makes a superconducting island.

to the charge on the parallel plates and is quantized with the following expression:

$$Q = 2q_e N. \quad (3.2)$$

Here, 2 is because two electrons are glued to each other to form a cooper pair and N stands for the number of cooper pairs in the island. Thus, the electrostatic energy of the capacitor is as follows:

$$E = \frac{Q^2}{2C}. \quad (3.3)$$

Here, Q is the total charge on the island and C stands for the capacitance of two islands. For the quantization of the CPB, we are considering $|N\rangle$ as the basis for the system. $|N\rangle$ is the many-particle ground state function which means all the cooper pairs are in the ground state. The charging energy of the CPB is given as:

$$\hat{H}_{charge} = \frac{\hat{Q}^2}{2C}. \quad (3.4)$$

The second term of the Hamiltonian deals with the exchange of the cooper pairs from one superconducting island to another and is given as:

$$\hat{H}_{exch} = \frac{-E_j}{2} \sum_{N=-\infty}^{\infty} \{|N+1\rangle \langle N| + |N\rangle \langle N+1|\}. \quad (3.5)$$

Here, E_j is the Josephson energy (depends upon the geometry and material properties) that gives strength to the tunneling of the Cooper pair. Therefore, the Hamiltonian of the two-level system (CPB) is given as follows:

$$\hat{H} = \frac{(\hat{Q} - Q_G)^2}{2C} - \frac{E_j}{2} \sum_{N=-\infty}^{\infty} \{|N+1\rangle \langle N| + |N\rangle \langle N+1|\}. \quad (3.6)$$

Here, Q_G is the gate charge which incorporates the external field through which

CPB is tuned by a relation $Q_G = C_G V_G$. Changing the electrostatic part of the Hamiltonian into the number of cooper pairs, $\hat{Q} = 2q_e \hat{N}$, we write the above Hamiltonian as follows:

$$\hat{H} = \frac{(\hat{N} - N_G)^2}{2C} - \frac{E_j}{2} \sum_{N=-\infty}^{\infty} \{|N+1\rangle\langle N| + |N\rangle\langle N+1|\}. \quad (3.7)$$

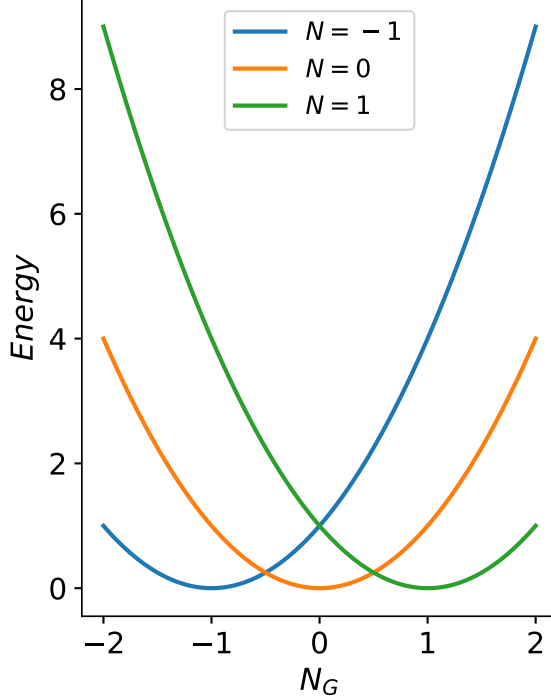


Figure 3.4: Graph of charging energy versus gate charge keeping the number of Cooper pair fixed at 1, 0, and -1. This graph is made considering the absence of tunneling term. Due to this fact, the degeneracy/crossings happen at various fractional intervals of gate charge. When we include the tunneling terms working as a perturbation, then these crossing becomes avoided crossing the same was happening in the study of a two-level system ref: chapter 2. Here $N=1$ means there are more Cooper pairs on the upper island and this graph can also be extrapolated for other N 's. In the avoided crossings, the lower branch from $N_G = \frac{1}{2}$ to $\frac{3}{2}$ for $N = 1$ worked as a ground state of the system.

In Fig. 3.4, we plot the energy of the CPB. We expand the charging Hamiltonian (square term) around $N_G = \frac{1}{2}$ by considering $N_G = \frac{1}{2} + \delta N_G$ and neglecting higher terms, the expression becomes:

$$(N - N_G)^2 = (N - \frac{1}{2} - \delta N_G)^2, \quad (3.8)$$

The charging energy of CPB becomes as:

$$E_{ch} = 4E_c(\frac{1}{4} \pm \delta N_G), + \text{ term for } N=0 \text{ and } - \text{ is due to } N=1.$$

Cancelling the energy offset E_c , we write down the given states as follows:

$$|N = 0\rangle \longrightarrow E_{ch} = 4E_c\delta N_G, \quad |N = 1\rangle \longrightarrow E_{ch} = -4E_c\delta N_G. \quad (3.9)$$

Taking Fock states as basis states, $|N = 0\rangle = \begin{pmatrix} 1 \\ 0 \end{pmatrix}$ and $|N = 1\rangle = \begin{pmatrix} 0 \\ 1 \end{pmatrix}$ and in presence of tunneling term, the Hamiltonian is:

$$H = 4E_c\delta N_G |0\rangle\langle 0| - 4E_c\delta N_G |1\rangle\langle 1| - \frac{E_j}{2}(|0\rangle\langle 0| + |1\rangle\langle 1|). \quad (3.10)$$

In matrix form, the above Hamiltonian follows as:

$$H = \begin{pmatrix} 4E_c\delta N_G & -\frac{E_j}{2} \\ -\frac{E_j}{2} & -4E_c\delta N_G \end{pmatrix} \quad (3.11)$$

After diagonalizing the given Hamiltonian, we get the eigenvalues of the system as follows:

$$E = \pm \sqrt{\frac{E_j^2}{4} + 16E_c^2\delta N_G^2}. \quad (3.12)$$

In Figure 3.5, it is clear when the Josephson energy (tunneling parameter) is zero, we get the straight lines crossing at the origin. This gives rise to a degeneracy point O at the origin for the basis states $|N = 0\rangle$ and $|N = 1\rangle$. But we need avoided crossings to use them as distinct states with distinct energy eigenvalues. This happens when we include the Josephson energy in the expression of the total energy of the TLA. The degeneracy of the states is disappeared and we get two states represented by points B and A which are the superposition of the given basis states. This graph is exactly similar to the energy levels of the two-level system that we studied in the start of Chapter 2.

3.2 Transmission Lines

The investigation into the adverse effects associated with various apparatus used for wave propagation has yielded significant discoveries that minimize adversities and offer valuable applications in the field of technology. One notable example is the utilization of fiber optics as a reliable medium for optical field transmission. However, when it comes to the transmission of microwave pulses, alternative materials are required that possess excellent conducting properties while effectively blocking any internal fields and avoiding interference with other equipment in the system.

Transmission lines have emerged as a viable solution with several advantages

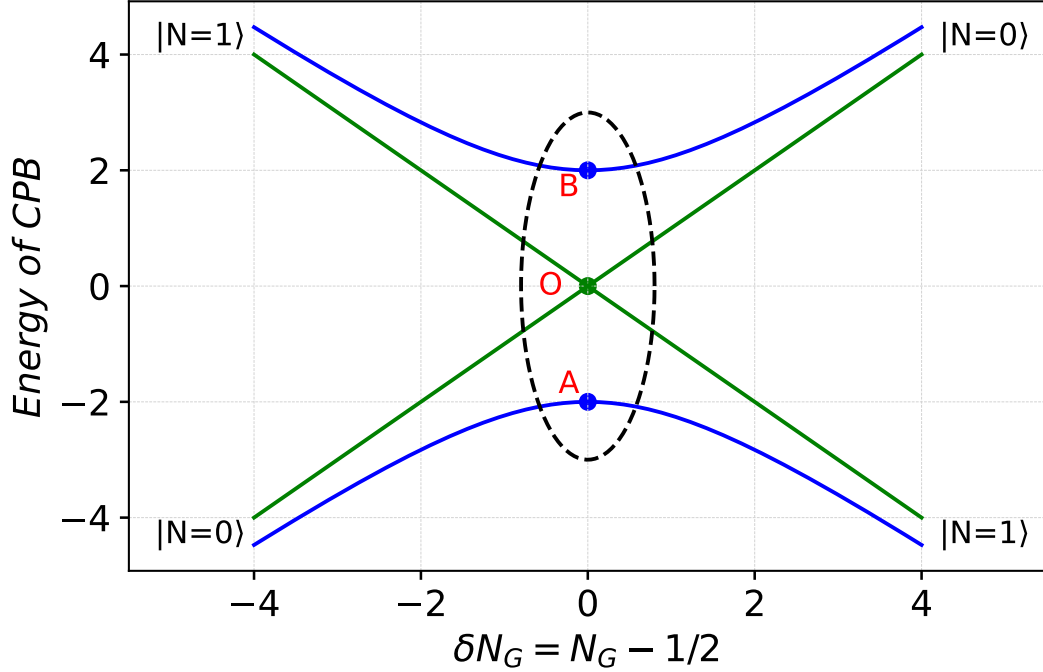


Figure 3.5: Graph of energy levels against the gate charge of Cooper pair box in the presence and absence of Josephson energy. The points A and B correspond to the superposition of given basis states and are equal to $\frac{1}{\sqrt{2}} \begin{pmatrix} 1 \\ 1 \end{pmatrix}$ and $\frac{1}{\sqrt{2}} \begin{pmatrix} 1 \\ -1 \end{pmatrix}$, respectively.

over the aforementioned examples. They serve as an efficient means of wave propagation and accurately be modeled as a collection of infinite inductor-capacitor oscillators. Microwave frequencies can readily pass through transmission lines, while also significantly reducing the impact of field effects on other components within the apparatus. The diagram 3.6 below illustrates the discretization of transmission lines, modeled as a network of LC oscillators.

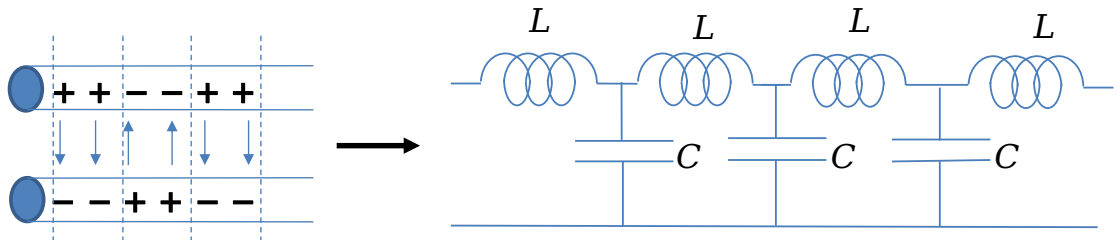


Figure 3.6: Schematic representation of the discretization of transmission lines into inductor-capacitor oscillators. Inductors are shown on the upper transmission line and the same is the case for the lower line but for the brevity of the analysis, we exclude them.

This approach showcases the ability of transmission lines to facilitate the smooth transmission of microwave pulses, safeguarding the integrity of the overall system and optimizing its performance.

3.2.1 Quantization of transmission lines

We have seen in the above section that the transmission lines can be modeled in terms of an infinite collection of capacitors and inductors. Following Fig. 3.7 shows one such illustration.

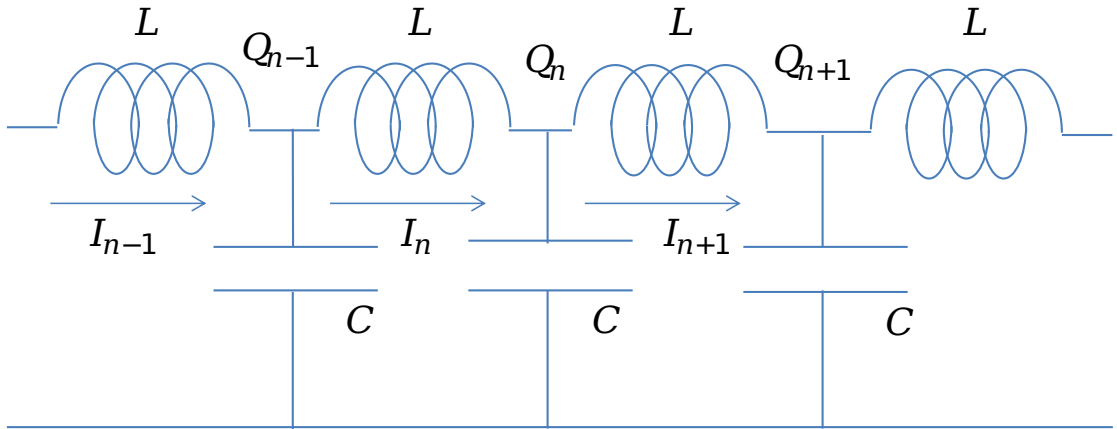


Figure 3.7: Transmission lines are discretized into n LC oscillators. Q_n is the amount of charge at the n th node and L is the value of self-inductance in the transmission line. I_n is the amount of current passing through the n th node.

We quantize the transmission lines as a Q.H.O. following the *Dirac criteria*. The LC oscillators have a quadratic potential term:

$$L = \frac{1}{2}LI^2 + \frac{1}{2C}Q^2. \quad (3.13)$$

Here, the first term corresponds to the energy of the inductor and the second term relates to the energy of the capacitor. Similarly, the position and momentum conjugate variables are given as: $P = \frac{\partial L}{\partial Q}$ which consequently equal to $P = \phi$. So the Hamiltonian $H = H(Q, \phi)$ is:

$$H = \frac{Q^2}{2C} + \frac{\phi}{2L}, \quad (3.14)$$

where $\phi = LI$ is the magnetic flux in the circuit. For simplicity in calculations and to get rid of an infinite sum problem for the current at each node, we take ϕ as a generalized coordinate and Q as a generalized momentum. Therefore, the Lagrangian of the full transmission lines is the sum of the Lagrangian of each capacitor-inductor model. The final form for the Lagrangian of the system as a whole, considering the expression for the current at each node $I_n = \frac{\phi_{n-1}-\phi_n}{L}$, is given as:

$$L = \sum_n \left[\frac{C}{2} \dot{\phi}^2 - \frac{(\phi_{n-1} - \phi_n)^2}{2L} \right]. \quad (3.15)$$

Similarly, the sum symbol can be changed as an integral with dx as a limit when there is a continuum case. We apply Legendre transformation to convert this discrete version case into the Hamiltonian. By considering the conjugate momentum $P_n = \frac{\partial L}{\partial \dot{\phi}_n} = Q_n$, the Hamiltonian is as follows:

$$H = \sum_n P_n \dot{\phi}_n - L. \quad (3.16)$$

This satisfies the commutation relation, thus, converting $\phi_n \leftrightarrow \hat{\phi}_n$ and $P_n \leftrightarrow \hat{P}_n$, and the Hamiltonain is derived as:

$$\hat{H} = \sum_n \left[\frac{\hat{P}_n}{2C} + \frac{(\hat{\phi}_{n-1} - \hat{\phi}_n)^2}{2L} \right]. \quad (3.17)$$

The form of Hamiltonian is quadratic in nature similar to a simple harmonic oscillator. Next, our job is to convert this form as a Q.H.O. form i.e. $a^\dagger a$. We have considered that the transmission line is translationally invariant and each cell (containing each model of capacitor-inductor) is equivalent. Next, exploit this invariance by choosing the normal coordinates as normal modes. Due to translational invariance, plane waves will be their normal modes. Taking the PBCs and from that periodicity, we have $e^{ikx} = e^{ik(x+W)}$ where W is the circumference of the above supposed periodic transmission line. By considering $e^{ikx} = 1 = e^{i2\pi n}$, the quantized momentum vector is as follows: $k_n = \frac{2\pi}{W}n$. To solve the above Hamiltonian, we consider the following *ansatz* for the magnetic flux:

$$\hat{\phi}_n = \sum_{-\frac{\pi}{2} \leq k \leq \frac{\pi}{2}} A_k (\hat{a}_k e^{ikx} + \hat{a}^\dagger e^{-ikx}). \quad (3.18)$$

Ansatz is the superposition of plane waves with A_k having a dimension of magnetic flux. We have taken the translation invariance as: $A_k = A_{-k}$ and $\omega_k = \omega_{-k}$. Similarly, the *ansatz* for the momentum coordinate $P_n = C\dot{\phi}_n$ is as follows:

$$\hat{P}_n = \sum_k CA_k^*(-i\omega_k) [\hat{a}_k e^{ikx} + \hat{a}^\dagger e^{-ikx}]. \quad (3.19)$$

This $-i\omega_k$ term is in accordance with the \hat{a}_k evolution as follows: $\hat{a}_k \propto e^{-i\omega_k t}$ given in the second chapter. Now plugging back the given ansatz for magnetic flux and momentum conjugate (P), we get a messy form of the final expression. We have three sum symbols $\sum_n \sum_k \sum_{k'}$ in the Hamiltonian. Like in P_n :

$$P_n^2 = \sum_k \sum_{k'} C^2 A_k A_{k'} (-\omega_k \omega_{k'}) [\hat{a}_k \hat{a}_{k'} e^{i(k+k')x} - h.c.], \quad (3.20)$$

we have two sum symbols which are tedious to evaluate the final expression. So, using the following orthogonality condition:

$$\sum_n e^{i(k+k')x} = \delta_{k,k'} \frac{W}{a}, \quad (3.21)$$

when $k \neq k'$, the above sum equals to zero, otherwise equals to $\frac{W}{a}$. Finally, we obtain the Hamiltonian in one \sum_k symbol. Here W is the circumference or the interval after which the wave vector repeats its values. Solving the whole Hamiltonian is a big task but through some substitutions, we have few useful results. For example, in the Hamiltonian, there is one term as a bilinear combination of annihilation operator which is not wanted.

$$a_k a'_k \frac{W}{a} A_k^2 \left[\frac{-C}{2} \omega_k^2 + \frac{2}{L} \sin^2\left(\frac{ka}{2}\right) \right]. \quad (3.22)$$

Ignoring this term, we obtain the following dispersion relation of a wave propagating over the transmission line:

$$\omega_k = \frac{2}{\sqrt{LC}} \left| \sin\left(\frac{ka}{2}\right) \right|. \quad (3.23)$$

This dispersion relation is shown below in Figure 3.8 which is very important in characterizing the material/system properties.

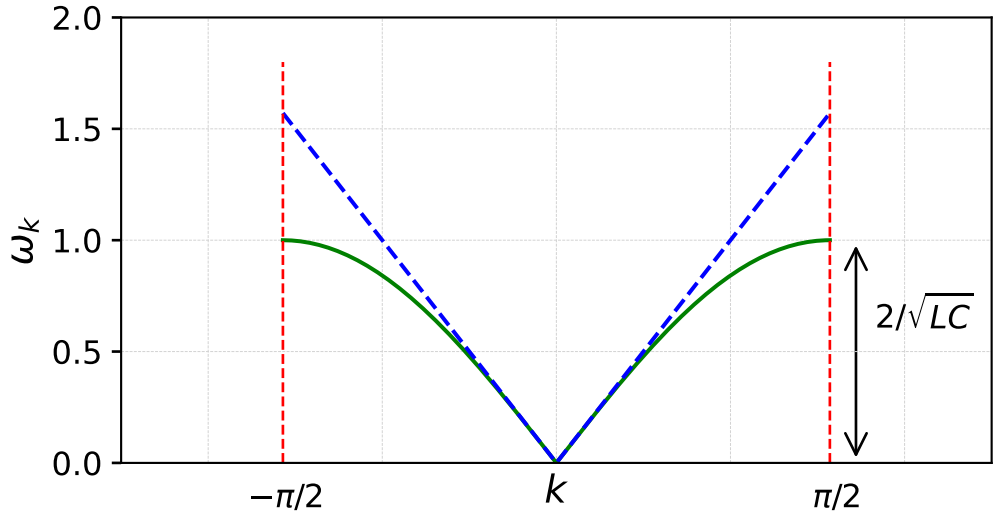


Figure 3.8: Graph of dispersion relation in the transmission lines. For smaller values of the wave vector, it behaves linearly but at larger wave vector values it becomes almost quadratic. The maximum height of ω_k at $k = \frac{\pi}{2}$ is $\frac{2}{\sqrt{LC}}$.

Similarly, the other terms in the Hamiltonian are as follows:

$$\hat{H} = \sum_k \frac{2W}{a} A_k^2 \left[\frac{C}{2} \omega_k^2 + \frac{2}{L} \sin\left(\frac{ka}{2}\right) \right] (\hat{a}_k^\dagger \hat{a}_k + \frac{1}{2}). \quad (3.24)$$

From the dispersion relation, setting $\frac{2}{L} \sin\left(\frac{ka}{2}\right) = \frac{C}{2} \omega_k^2$ and plugging back in one of the terms of Hamiltonian. Along with this, substituting $c = \frac{C}{a}$ and $A_k = \sqrt{\frac{\hbar}{2C_{full}\omega_k}}$ where $C_{full} = cW$ is the capacitance of full transmission line. Finally, upon these substitutions, we get the Hamiltonian in the following form:

$$\hat{H} = \sum_k \hbar \omega_k (\hat{a}_k^\dagger \hat{a}_k + \frac{1}{2}). \quad (3.25)$$

The transmission lines look like a collection of independent Q.H.O. Similarly, CPB is coupled with an external voltage, and in practical applications we usually tune the CPB through this voltage. So, the expression for the voltage $V = \dot{\phi}$ in terms of annihilation and creation operator is given below:

$$\hat{V}(x) = \sum_k \sqrt{\frac{\hbar}{2C_{full}\omega_k}} (-i\omega_k) [\hat{a}_k e^{ikx} - \hat{a}_k^\dagger e^{-ikx}]. \quad (3.26)$$

3.2.2 Model the Hamiltonian of transmission line resonators

Making a cut-off to the transmission lines makes it a resonator because few number of modes can reside in that length of the transmission line. Field passes through it makes a standing wave pattern and acts as a transmission line resonator. Instead of PBCs as in the case of transmission lines, we have boundary conditions: $I(x = -\frac{d}{2}, \frac{d}{2}) = 0$. Consequently, the change in magnetic flux at the node is $\phi_{n-1} - \phi_n = LI_n$. The normal modes are the collection of standing waves. Similarly, supposing an *ansatz* to solve the given Hamiltonian using the above-mentioned boundary conditions:

$$\hat{\phi}_n(x) = \sum_{n=1}^{\infty} A_n \phi_n(x) (\hat{a}_n^\dagger + \hat{a}_n), \quad (3.27)$$

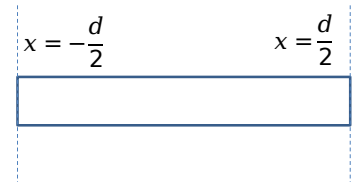


Figure 3.9: Schematics of the transmission line resonator with the given boundary conditions

where the given $\phi_n(x)$ is given below:

$$\phi_n(x) = \begin{cases} \sin\left(n \frac{\pi}{d} x\right), & n = 1, 3, 5, \dots, \\ \cos\left(n \frac{\pi}{d} x\right), & n = 2, 4, 6, \dots \end{cases} \quad (3.28)$$

Similarly, we have one for the momentum conjugate:

$$\hat{\pi}(x) = \sum_{n=1}^{\infty} A_n \phi_n(x) (-i\omega_n) (\hat{a}_n - \hat{a}_n^\dagger). \quad (3.29)$$

Plugging back the given *ansatzes* in the expression of the Hamiltonian, we have performed the same calculations here as did for the case of transmission lines. Following that, one special condition is the use of orthogonality condition and the substitution of the prefactor $A_n = \sqrt{\frac{\hbar}{C_{full}\omega_n}}$ where $C_{full} = cd$ and $c = \frac{Capacitance(C)}{unit\ length(a)}$, we obtain the following form of the Hamiltonian:

$$\hat{H} = \sum_n \hbar\omega_n (\hat{a}_n^\dagger \hat{a}_n + \frac{1}{2}). \quad (3.30)$$

Thus, TLR are modeled as the collection of independent quantum harmonic oscillators. As the given resonator is coupled through the external voltage, the expression for the voltage is given below after considering the transformation that momentum and coordinate have equal weightage in Hamiltonian:

$$\hat{V}(x) = \sum_n \omega_n A_n \phi_n(x) (\hat{a}_n + \hat{a}_n^\dagger). \quad (3.31)$$

3.2.3 Cooper Pair Box coupled with external voltage

In this subsection, we derive the interaction Hamiltonian when CPB is coupled with the TLR through an external voltage. Earlier we know that an electric field is used to tune the CPB and $E_{ex} \propto V(x)$. So, interaction Hamiltonian is as follows when CPB is put inside the external electric field \vec{E}_{ext} :

$$\bar{H}_{int} = -\bar{\mu} \cdot \vec{E}_{ext}. \quad (3.32)$$

Here, $\bar{\mu}$ is the dipole moment of the CPB. We already know the fluctuating charge term, $\delta\hat{Q}_G$ in the expression for the Hamiltonian of the CPB in the previous section, which can be written as $\delta\hat{Q}_G = C_G \hat{V}(x)$. Plugging these values in CPB Hamiltonian, and canceling the offsets, we have the interaction term as follows:

$$\hat{H}_{int} = \frac{-C_G}{C} (\hat{Q} - Q_G) \dot{\hat{V}}(x). \quad (3.33)$$

This is the final expression that depicts the coupling of the CPB with the external voltage. Taking only the single mode of voltage, the interaction Hamiltonian

becomes as follows:

$$\hat{H}_{int} = \frac{-C_G}{C} \omega_n A_n \phi_n(x) (\hat{Q} - Q_G) (\hat{a}_n + \hat{a}_n^\dagger). \quad (3.34)$$

Considering the charge operator in terms of number operator \hat{N} and taking only ground state and 1st excited state with $N_G = \frac{1}{2}$ as follows:

$$|g\rangle = \frac{1}{\sqrt{2}}(|N=0\rangle + |N=1\rangle) \quad |e\rangle = \frac{1}{\sqrt{2}}(|N=0\rangle - |N=1\rangle). \quad (3.35)$$

Now using the above states as basis states and expanding the number operator $\hat{N} - N_G$ in terms of these basis states as follows:

$$\begin{aligned} \hat{N} - N_G = & \langle g | \hat{N} - N_G | g \rangle \langle g | g \rangle \\ & + \langle e | \hat{N} - N_G | e \rangle \langle e | e \rangle \\ & + \langle g | \hat{N} - N_G | e \rangle \langle g | e \rangle \\ & + \langle e | \hat{N} - N_G | g \rangle \langle e | g \rangle. \end{aligned} \quad (3.36)$$

So, with $N_G = \frac{1}{2}$, we are only interested in the cross terms of number operators which are actually giving a sense of inversion between excited and ground state, then the interaction Hamiltonian is:

$$\hat{H}_{int} = \hbar g \hat{\sigma}_x (\hat{a}_n + \hat{a}_n^\dagger). \quad (3.37)$$

Here, $\hbar g = \frac{C_G}{C} \omega_n A_n \phi_n(x) q_e$ and g is with the dimension of frequency known as coupling parameter/coefficient. The parameter g gives the coupling strength between the artificial atom (CPB) and the TLR. Its value commonly is in the range of few *MHz* to 100 *MHz*. This general interaction Hamiltonian (called **Jaynes Cummings Model**) describes how an artificial atom (TLA, CPB) gets coupled with the transmission line resonators through an applied external electric field.

3.3 The Jaynes Cummings (JC) Model

JC model describes the interaction between an atom with the single mode field. In our case, an atom is coupled with TLR through an externally applied electric field as shown in the following Figure 3.10.

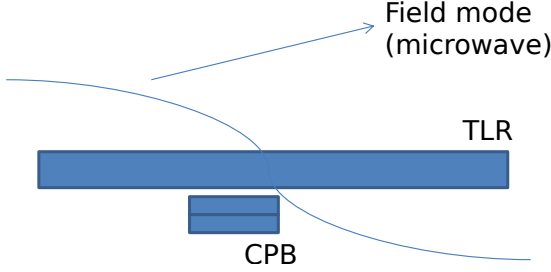


Figure 3.10: Schematic representation of the Cooper Pair Box when it is coupled with single mode microwave field. This field helps to tune the given artificial atom.

The full Hamiltonian of JC model by taking the two-level atom's energies ($|0\rangle = -\frac{\hbar\omega_{at}}{2}$, $|1\rangle = \frac{\hbar\omega_{at}}{2}$) is written as follows:

$$\hat{H}_{JC} = \hbar\omega\hat{a}^\dagger\hat{a} + \hbar\omega_{at}\frac{\hat{\sigma}_z + 1}{2} + \hbar g\hat{\sigma}_x(\hat{a}_n + \hat{a}_n^\dagger). \quad (3.38)$$

If $\hat{\sigma}_z = +1$ or -1 , the atom is in the excited or ground state, respectively. JC model does not have exact analytical solutions but it is solved by using some approximations. Those approximations are RWA and weak field limit. This weak field is determined through the small value of coupling constant g and due to having this small parameter, the last term in the Hamiltonian of the JC model can be taken as a perturbation. When $g = 0$, it means that there is no interaction between the atom and resonator and the energy levels of the atom and field will remain the same in this case (which means levels do not split due to not having any perturbation). The Hamiltonian of JC model under RWA is given by:

$$\hat{H}_{JC,RWA} = \hbar\omega\hat{a}^\dagger\hat{a} + \hbar\omega_{at}\frac{\hat{\sigma}_z + 1}{2} + \hbar g(\sigma_+\hat{a}_n + \sigma_-\hat{a}_n^\dagger). \quad (3.39)$$

Here, for $n = 1$, $\sigma_+\hat{a}$ tells that atom is raised from the ground state to the excited state and a photon is absorbed. Similarly, $\sigma_-\hat{a}^\dagger$ tells that the atom is de-exciting $|1\rangle \rightarrow |0\rangle$, and a photon is created. σ_- and σ_+ are the atomic lowerig and raising operator, respectively. The interaction part of the Hamiltonian contains terms like $\sigma_+\hat{a}$ and $\sigma_+\hat{a}^\dagger$ which we ignore under RWA because these do not describe any physical phenomenon and correspond to fast oscillating terms in the classical case.

Now taking the case when the coupling parameter is not zero then energy levels will shift upward in the energy level diagram, as shown below in Fig. 3.11, due to the perturbation term in the Hamiltonian. From the Fig. 3.11, it is clear that interaction is between $|\downarrow, n\rangle \leftrightarrow |\uparrow, n-1\rangle$ and we have neglected the off-resonant terms because their effects are tiny. $|\downarrow, n\rangle$ means that the atom is de-excited and a photon is created while $|\uparrow, n-1\rangle$ means that atom is excited and a photon is absorbed. Considering only these as the basis states and Hamiltonian of JC model

under RWA is written in matrix form as follows:

$$\hat{H} = \sum_{i,j} |i\rangle \langle i| \hat{H}_{JC,RWA} |j\rangle \langle j|. \quad (3.40)$$

Here, $|i\rangle$ and $|j\rangle$ stands for basis states which are $|\alpha\rangle = |\downarrow, n\rangle$ and $|\beta\rangle = |\uparrow, n-1\rangle$. So, under RWA, the final form of Hamiltonian in the matrix notations is:

$$\hat{H} = \begin{pmatrix} H_{\alpha\alpha} & H_{\alpha\beta} \\ H_{\beta\alpha} & H_{\beta\beta} \end{pmatrix}. \quad (3.41)$$

After applying the corresponding elements of the given matrix Hamiltonian on each basis states, we get the expression for the JC Hamiltonian as follows:

$$\hat{H}_{JC,RWA} = \begin{pmatrix} \hbar\omega n & \hbar g \sqrt{n} \\ \hbar g \sqrt{n} & \hbar\omega n + \hbar\Delta \end{pmatrix} \quad (3.42)$$

Here $\Delta = \omega_{at} - \omega$ is the detuning factor. After diagonalizing the given Hamiltonian, we obtain its eigenvalues as follows:

$$E_{\pm} = \hbar\omega n + \frac{\hbar\Delta}{2} \pm \hbar\sqrt{g^2n + (\frac{\Delta}{2})^2}. \quad (3.43)$$

In the resonant case when the difference between the frequency of the field, and the difference of energy between the energy levels of an artificial atom is zero such that $\Delta = 0$, the eigenenergies are as:

$$E_{\pm}^n = \hbar\omega n \pm \hbar g \sqrt{n}. \quad (3.44)$$

The energy levels of the artificial atom get split which is more clearly shown in the diagram 3.11 below.

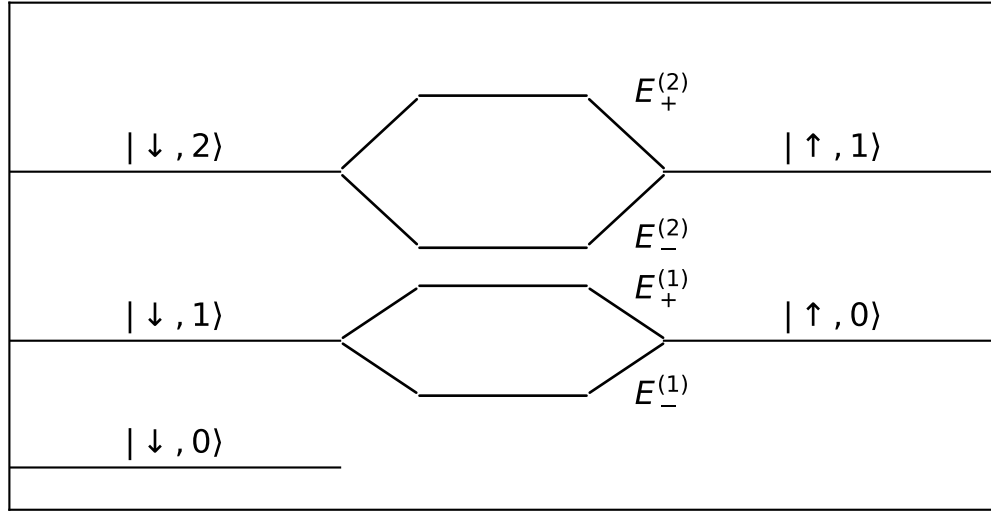


Figure 3.11: Schematic representation of the splitting of the energy levels. $|\downarrow, 1\rangle$ energy level is splitted into two eigenenergies $E_{\pm}^{(1)} = \hbar\omega \pm \hbar g$ with an energy gap $= 2\hbar g$. Similarly, the energy level $|\downarrow, 2\rangle$ is further separated to $E_{\pm}^{(2)} = 2\hbar\omega \pm \hbar g\sqrt{2}$ with a gap $= 2\sqrt{2}\hbar g$.

3.3.1 Rabi oscillations

We have derived the Hamiltonian \hat{H} in the above sections but have not studied the dynamics of the system yet. Say at a time, $t = 0$ the atom is in the ground state and the photon is in field mode. Considering the following eigenstates with the corresponding eigenenergies:

- $\frac{1}{2} |\downarrow, n\rangle + |\uparrow, n-1\rangle$
 $E_+ = \hbar\omega n + \hbar g\sqrt{n}$
- $\frac{1}{2} |\downarrow, n\rangle - |\uparrow, n-1\rangle$
 $E_- = \hbar\omega n - \hbar g\sqrt{n}$

At some later time t , the eigenstate after evolution will be in some of the superposition states which is given as follows:

$$|\psi(t)\rangle = \frac{1}{2} |\downarrow, n\rangle + |\uparrow, n-1\rangle \exp\left\{\frac{-i}{\hbar} E_+ t\right\} + \frac{1}{2} |\downarrow, n\rangle - |\uparrow, n-1\rangle \exp\left\{\frac{-i}{\hbar} E_- t\right\}. \quad (3.45)$$

Now finding out the probabilities $P_{\downarrow}(t)$ which is the probability of the atom being in the ground state. Taking modulus squares of the wavefunction, we get the expression for probabilities as follows:

$$P_{\downarrow}(t) = \frac{1}{2}(1 + \cos(2g\sqrt{n}t)). \quad (3.46)$$

When $P_{\downarrow}(t) = 0$ means that one photon from the field mode is getting converted to one excitation in the atom. Following is the plot (see Fig. 3.12) between probability $P_{\downarrow}(t)$ and time t which are commonly called **Rabi oscillations**.

Here $g\sqrt{n}$ is the Rabi frequency related to field amplitude and n is the number of photons in the field mode. If $n = 0$, then the transitions are termed as vacuum Rabi oscillations but if $n \gg 1$, then it is the classical case and Rabi frequency will also behave classical.

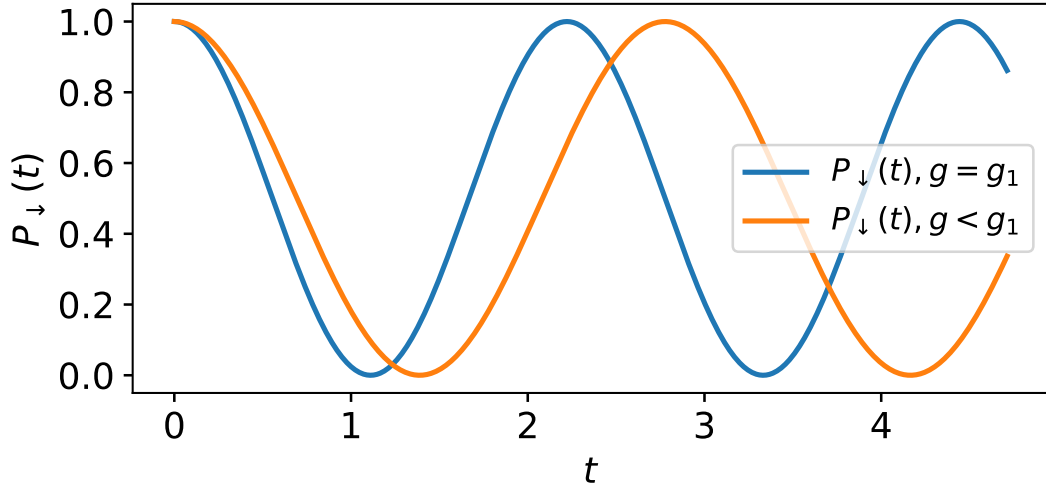


Figure 3.12: Graph of Rabi oscillation showing the transition probabilities. The Blue lines represent the transition probabilities at some coupling parameters but the orange line depicts the case when the coupling constant is lowered than the previous and thus, found transition probabilities are having low rates.

3.3.2 Dispersive case when $|\Delta| \gg g$

When the coupling strength between the field and the atom is very small, then the frequency of the field mode depends on the states of the atom. This implies that we can determine the state of the atom just by measuring the frequency of the field without directly altering or measuring the state of an atom. This same procedure is followed in the measurement of an artificial atom in a quantum computing processor. The case when $|\Delta| \gg g$ is called the dispersive case. To solve the Hamiltonian of JC model 3.39 under the dispersive case, expanding the expression of eigenenergies of the Hamiltonian and excluding the higher order terms, we obtain:

$$E_+ = \hbar(\omega + \frac{g^2}{|\Delta|})n + \hbar\Delta \quad E_- = \hbar(\omega - \frac{g^2}{|\Delta|})n. \quad (3.47)$$

E_+ is the excited state and E_- is the ground state. Frequencies of the equally spaced two harmonic oscillators are given by $\omega + \frac{g^2}{|\Delta|}$ and $\omega - \frac{g^2}{|\Delta|}$. While during spectroscopy in the experiment, if field frequency is measured and it happens to be greater than ω then an atom is thought to be in the excited state, and vice versa. As we already know that $\sigma_z = \pm 1$ refer to $|\uparrow, n-1\rangle$ and $|\downarrow, n\rangle$ respectively. So, the effective Hamiltonian for this case will be:

$$H_{eff} = \hbar(\omega + \frac{g^2}{|\Delta|}\hat{\sigma}_z)\hat{a}^\dagger\hat{a} + \hbar(\omega_{at} + \frac{g^2}{|\Delta|})\frac{\hat{\sigma}_z + 1}{2}. \quad (3.48)$$

This is clearly observed in an experiment conducted by Wallraff et al. [1] at Yale University.

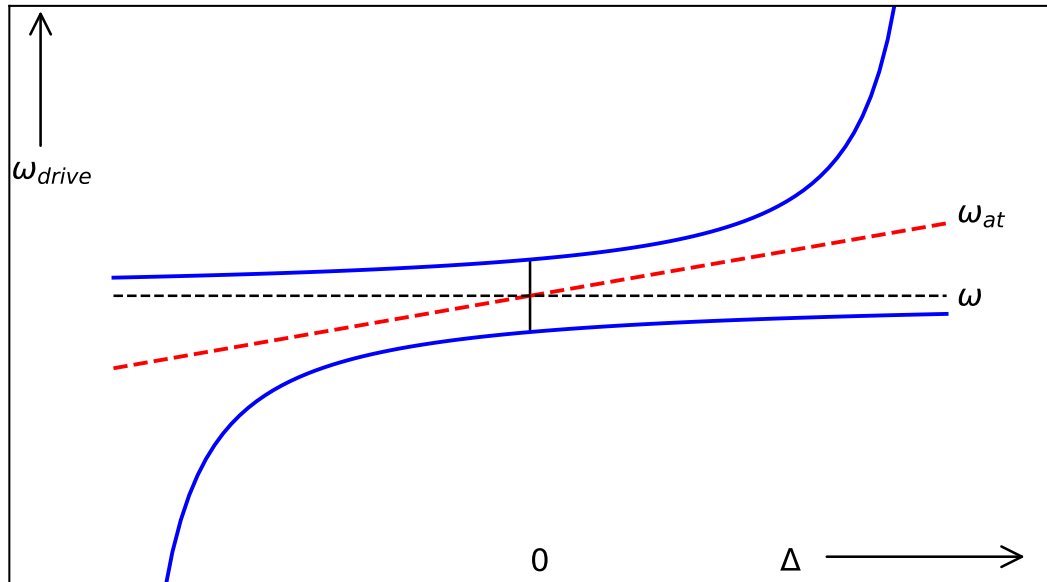


Figure 3.13: Graph representing the relation of frequency of drive field on-chip microwave resonator against the detuning parameter and ω is the bare cavity frequency. Figure elaborates that how atomic frequency gets lifted and shows two peaks due to the shift in the frequency and the details can be seen in Wallraff research work [1].

3.4 Josephson Junctions

The story of the SC junction goes back to the results of the Ginzburg-Lindau (GL) theory for superconductivity which is the basis for other valid theories of superconductivity i.e. BCS theory. GL theory states that the wavefunction $|\psi(r, t)\rangle$ describes the behavior of an ensemble of SC electrons so-called cooper pairs, all having the same phase. The local density of SC electrons is calculated from the subsequent expression: $n_s(r, t) = |\psi(r, t)|^2$. JJ is a type of junction consisting of two SC islands and an insulating material sandwiched between them. Figure 3.14

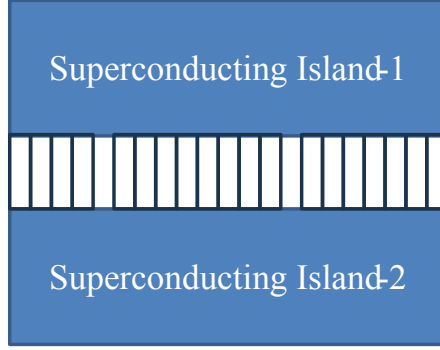


Figure 3.14: Josephson Junction, consists of two Superconducting (S.C.) islands (Al) separated by an insulating material, in this case, Al_2O_3 .

shows schematics of a typical JJ. This junction exhibits very important and novel characteristics i.e. flow of electrons even in the absence of potential, and it is the main ingredient in SC QC processors.

3.4.1 Flux quantization

Flux enclosed by a superconductor must be quantized in units of flux quantum $\Phi_o = \frac{\hbar}{2e}$. From the amperes law for the conservative field, we have

$$\oint_C J_s \cdot dl = 0. \quad (3.49)$$

Putting the expression for the current density J_s calculated from the continuity equation, we get the following expression:

$$\oint_C \hbar \bar{\nabla} \theta(r, t) \cdot dl = \oint_C \hbar q A \cdot d\bar{l} \quad (3.50)$$

Here, phase $\theta_o(r, t)$ is not well defined, so taking a general phase into account and using the subsequent wavefunction: $\psi(r, t) = \sqrt{n_s(r, t)} e^{i(\theta_o(r, t) + 2n\pi)}$. Now, the left-hand side of the above equation will give us $2n\pi\hbar$ and the right-hand side will give us $q\Phi_B$ by using the Stokes theorem. We obtain the quantization as follows:

$$\Phi_B = \frac{\hbar}{2e} n \quad \longrightarrow \quad \Phi_B = n\Phi_o. \quad (3.51)$$

Here, Φ_o is flux quantum which delineates the discreteness of the magnetic flux in a superconducting ring and $2e$ is due to cooper pair containing two electrons.

3.4.2 Nonlinear effects of Josephson junctions

Josephson's effect was discovered by Brian D. Josephson. It is a coherent phenomenon that predicts supercurrent flow between two superconductors separated by an insulating layer, thin enough for the e^- pairs to tunnel through. The dynamics of the JJ is explained through the following differential equations:

$$i\hbar \frac{\partial \psi_1}{\partial t} = U_1 \psi_1 + a \psi_2 \quad i\hbar \frac{\partial \psi_2}{\partial t} = U_2 \psi_2 + a \psi_1. \quad (3.52)$$

Here, the first equation containing the ψ_1 describes the tunneling dynamics from the first region, and the second equation having the state function ψ_2 delineates the dynamics behind the tunneling from the second region to the first one. U_1 and U_2 are the ground state energies of each superconductor and a is a coupling parameter that characterizes the overlap between the wavefunction. If $a = 0$, we have uncoupled wavefunctions which means an insulating layer is thick enough that tunneling does not occur. To solve the above equation and find out the dynamics, let us suppose we have the following two many-particle wavefunctions:

$$\psi_1 = \sqrt{n_1(\bar{r}, t)} e^{i\theta_1(\bar{r}, t)} \quad \psi_2 = \sqrt{n_2(\bar{r}, t)} e^{i\theta_2(\bar{r}, t)}. \quad (3.53)$$

Here, n_1 and n_2 are the local density of cooper pairs in superconductors 1 and 2 respectively, and θ_1 and θ_2 are the phases of each superconductor. So, plugging these wavefunctions into the above Schrodinger equations and after comparing real and imaginary parts, we obtain a total of four equations. Equating the imaginary part of the equations, we get the following expression for the derivative of local density:

$$\dot{n}_1 = \dot{n}_2 = \frac{2a}{\hbar} \sqrt{n_1 n_2} \sin(\theta_2 - \theta_1). \quad (3.54)$$

This is the relation between super current density and phase difference across the junction which shows that it varies sinusoidally. If as an example considering $n_1 \sim n_2 = n$, then we have Josephson current as follows:

$$J_s = J_c \sin(\phi) \quad (3.55)$$

Here, $J_c = \frac{2qan}{\hbar}$ is the critical density and ϕ is the difference of two phases. As we know from the inductance vs voltage relation that $L = \frac{V}{I}$, Josephson junction is equivalent to a non-linear inductor with inductance $L_J = \frac{V}{I}$. We also have an idea about the Josephson current from the above relations.

$$I = I_c \sin(\phi) \quad (3.56)$$

I_c is the critical current through the junction. So, taking its derivative w.r.t ϕ and plugging back in the Josephson inductor relation and considering $\dot{\phi} = \frac{q}{\hbar}V$, we reach the following relation:

$$L_J = \frac{\hbar}{2\pi q I_c \cos(\phi)}. \quad (3.57)$$

where ϕ is the phase difference across the junction. This equation confirms that JJ has nonlinear inductance.

3.4.3 Hamiltonian of Josephson Junctions

To deduce the expression for the Hamiltonian of the JJ being discussed above, we know that the energy operator for a Josephson element is deduced from the discreteness of charge/cooper pairs that tunnel through the junction such that $Q_J = qN(t)$, Here $q = 2e$ and the number operator in the basis of number state or fock state is given as $\hat{N} = \sum_N N |N\rangle \langle N|$. Considering $N(t)$ as an operator whose eigenstates correspond to the macroscopic state of a circuit with a well-defined number of cooper pairs. The Josephson Hamiltonian in the fock basis is given by the following relation.

$$\hat{H}_J = \frac{-E_j}{2} \sum_{N=-\infty}^{\infty} \{|N+1\rangle \langle N| + |N\rangle \langle N+1|\}, \quad (3.58)$$

where Josephson energy is $E_j = \frac{\Phi_0 I_c}{2\pi}$. This Josephson Hamiltonian can be written in terms of phase difference. Introducing a new basis in terms of ϕ as follows:

$$|\phi\rangle = \sum_{N=-\infty}^{\infty} e^{iN\phi} |N\rangle. \quad (3.59)$$

This is periodic with a period 2π i.e. changing $\phi \rightarrow \phi + 2\pi$, $|\phi\rangle$ remains unchanged. Plugging the state basis in the form of an integral sign from the above $|\phi\rangle$ basis into Josephson Hamiltonian, we get H_J as follows:

$$H_J = \frac{-E_j}{2} \left[\frac{1}{2\pi} \int_0^{2\pi} e^{i(N+1)\phi} e^{-iN\phi} dx |\phi\rangle \langle \phi| + e^{-i(N+1)\phi} |\phi\rangle \frac{1}{2\pi} \int_0^{2\pi} e^{iN\phi} dx \langle \phi| \right]. \quad (3.60)$$

Introducing new operator $e^{i\hat{\phi}} = \frac{1}{2\pi} \int_0^{2\pi} e^{i\phi} dx |\phi\rangle \langle \phi|$, we can write the Hamiltonian of tunneling part of the Josephson element in a concise format as follows:

$$H_J = -E_j \cos(\hat{\phi}). \quad (3.61)$$

Here, $\hat{\phi}$ is the phase conjugate of the number operator \hat{N} . These both are conjugate variables through the subsequent commutation relation: $[\hat{\phi}, \hat{N}] = i$. This commutation relation suggests that the number operator couples linearly with the voltage operator through the cooper pair charge $2e$. We can also deduce the result that voltage is linearly coupled with phase difference with the following relation:

$$\phi(t) = \phi_o + \frac{q}{\hbar} \int V(t). \quad (3.62)$$

Figure 3.15 shows that JJ is modeled as having a capacitor with a nonlinear inductance.

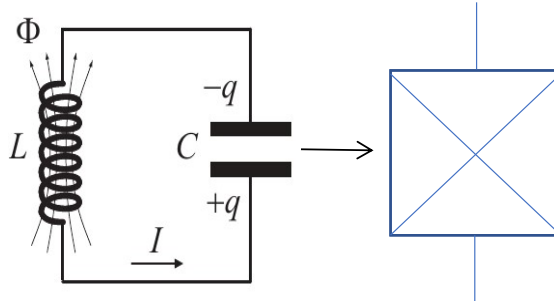


Figure 3.15: Circuit diagram of Josephson Junction exhibiting the nonlinear inductance with the shunted capacitance. The box containing a cross sign is the circuit symbol for the Josephson junction.

3.5 Types of Superconducting Qubit

Josephson junction is a non-linear inductor with a shunted capacitor. While plotting the energy levels on the potential diagram as shown in figure 3.16, we only take the lowest two levels to consider it as a non-linear harmonic oscillator. The final form of the Hamiltonian of Josephson junction is given by:

$$H = E_c N^2 - E_J \cos\left(\frac{\Phi}{\Phi_o}\right). \quad (3.63)$$

Here, Φ is the magnetic flux, and Φ_o is the flux quantum. This Hamiltonian is derived from taking the charging energy part where $Q = 2eN$ and $E_c = \frac{(2e)^2}{2C_J}$ into account and the tunneling part. E_c is the charging energy while E_J is the Josephson energy. There are three main types of SC qubits which are differentiated by the value of the ratio of Josephson energy to charging energy.

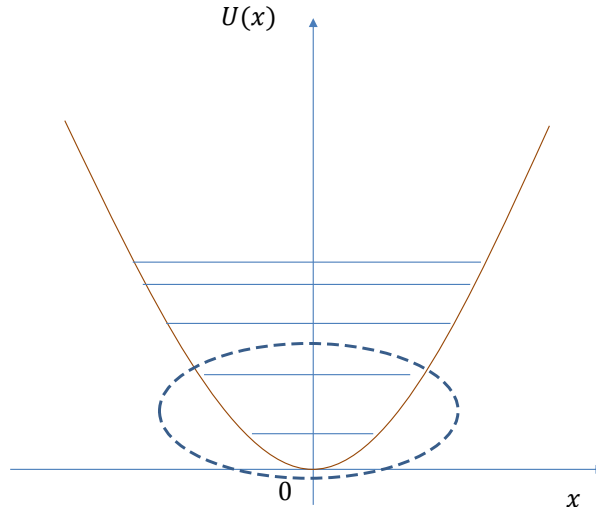


Figure 3.16: Representation of the nonlinear energy levels of Josephson junction on the position-dependent potential. The first two energy levels are considered as a two-level atom. The lowest and upper levels correspond to the ground and excited states, respectively.

3.5.1 Charge Qubit

Here, $\frac{E_J}{E_c} < 1$ means that charging energy dominates over the flux energy (Josephson energy) which further means that charge contributes significantly over the flux. This charge qubit is controlled by the applied external voltage as we have studied earlier about the Cooper pair box. The circuit diagram is given below in figure 3.17.

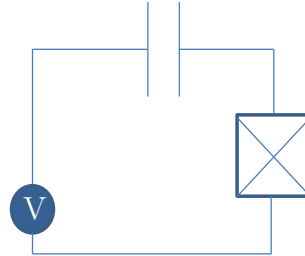


Figure 3.17: Circuit diagram of charge qubit/cooper pair box containing one Josephson junction and tuned through an external voltage.

3.5.2 Phase Qubit

Here, $\frac{E_J}{E_c} > 1$ means that Josephson energy dominates over the charging part. It is coupled with the external magnetic field, that is magnetic flux Φ_e , that flows across the closed loop and this flux includes 2-circulating super current states either counterclockwise or in a clockwise direction. The circuit diagram is given below in figure 3.18.

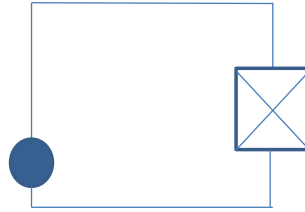


Figure 3.18: Circuit diagram of phase qubit containing a Josephson junction element with an external electrical current source

3.5.3 Flux Qubit

Here, $\frac{E_J}{E_c} \gg 1$ (roughly ~ 50) means that the Josephson part is significantly higher than the charging part. In this single JJ is connected to the current which plays with the phase difference in each part of the junction. The circuit diagram is given below:

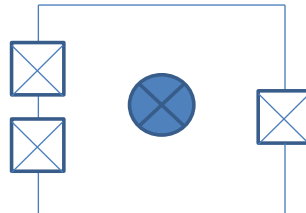


Figure 3.19: Circuit diagram of flux qubit containing three JJ and is coupled with the external magnetic field (into the page).

3.6 Transmon Qubit

Transmon qubit is widely used in the hardware for quantum computing and it resembles a charge qubit. It contains two JJ parallel to each other. Following Figure 3.20 shows its physical realization on the chip and the circuit mechanism behind its operation. The whole structure of transmon or any qubit can be elucidated by the following four terms: $Q(t)$, $i(t)$, $V(t)$, and magnetic flux $\Phi(t)$. These quantities are related to each other by some relations as already given in the aforementioned sections of this chapter. The whole junction can be represented as an energy function that has a dependence on the charge in magnetic flux across the two terminals. Josephson energy in terms of generalized magnetic flux is given below:

$$E(\Phi_J) = -E_J \cos\left(\frac{\Phi_J}{\Phi_o}\right). \quad (3.64)$$

Here, E_J is the Josephson tunneling energy and Φ_o is scaled in terms of magnetic flux which roughly is equal to $\frac{h}{2e} \sim 10^{-16}$ wb.

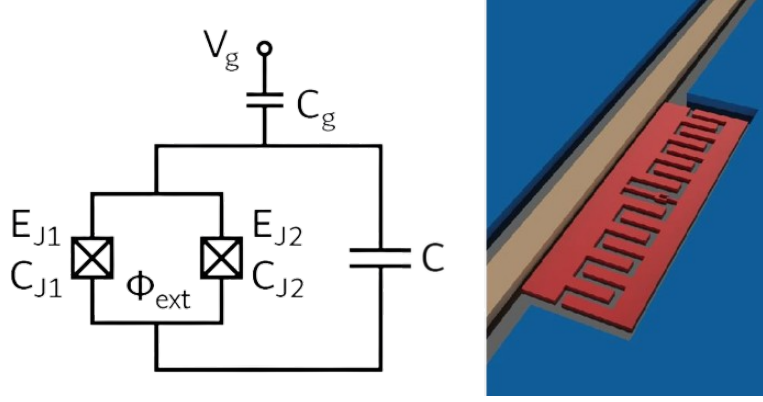


Figure 3.20: Representation of the transmon qubit on a superconducting chip having an array-like structure (right). Left is the details of the connection of the circuit components.

3.6.1 Hamiltonian of Transmon qubit

To drive the Hamiltonian of the Transmon qubit, we know that it consists of a charging energy term and nonlinear tunneling term as follows:

$$\hat{H} = \frac{\hat{Q}}{2C} - E_J \cos\left(\frac{\hat{\Phi}_J}{\Phi_o}\right). \quad (3.65)$$

Expanding the *cosine* term and ignoring the higher order terms and energy shift E_J , we write out the Hamiltonian, with a substitution $E_J \frac{\Phi_J^2}{2\Phi_o^2} = \frac{\Phi_J^2}{2L_J}$ where the linear effective inductance is $L_J = \frac{\Phi_o^2}{E_J}$, as follows:

$$\hat{H} = \frac{\hat{Q}^2}{2C} + \frac{\Phi_J^2}{2L_J} - \frac{E_J}{4!} \left(\frac{\Phi_J}{\Phi_o}\right)^4. \quad (3.66)$$

The first two terms in the above expression correspond to a linear harmonic oscillator while the last term corresponds to a non-linear harmonic oscillator. So, by the analogies, we say that Φ_J (magnetic flux) is the generalized coordinate. Using the definitions of the annihilation and creating operator, we write the magnetic flux in terms of the annihilation and creation operator as follows:

$$\Phi_J = \Phi_{ZPF}(\hat{a} + \hat{a}^\dagger). \quad (3.67)$$

Here, Φ_{ZPF} is the zero point fluctuation that is used for the normalization factor as we did in the quantization of CPB in the previous section. Similarly, the Hamiltonian is written in terms of annihilation and creation operators as follows:

$$\hat{H} = \hbar\omega_o \hat{a}^\dagger \hat{a} - \frac{E_J}{4!} \phi_{ZPF}^4 (\hat{a} + \hat{a}^\dagger)^4. \quad (3.68)$$

where $\omega_o = \frac{1}{\sqrt{L_J C}}$ and $\phi_{ZPF} = \frac{\Phi_{ZPF}}{\Phi_o}$. Expanding the given Hamiltonian and invoking the RWA by neglecting all rotating terms and keeping only non-rotating terms, we write the given Hamiltonian, with the substitutions of new terms $\hbar\alpha = \frac{E_J}{2}\phi_{ZPF}^4$ and $\hbar\alpha = \hbar\Delta q$, as follows:

$$\hat{H}_{RWA} = \hbar(\omega_o - \Delta q)\hat{a}^\dagger\hat{a} - \frac{\hbar\alpha}{2}\hat{a}^\dagger\hat{a}^2. \quad (3.69)$$

This is the Transmon Hamiltonian and $\omega_o - \Delta q = \omega_q$ is the Lamb shift (purely due to quantum fluctuations) which is due to normalized zero-point fluctuations of the magnetic flux. The second term in the above Hamiltonian is completely due to non-linearity. The graph of Josephson energy versus reduced magnetic flux $\frac{\Phi}{\Phi_o}$ is given below in Figure 3.21 which is representing the linear and non-linear parts more explicitly.

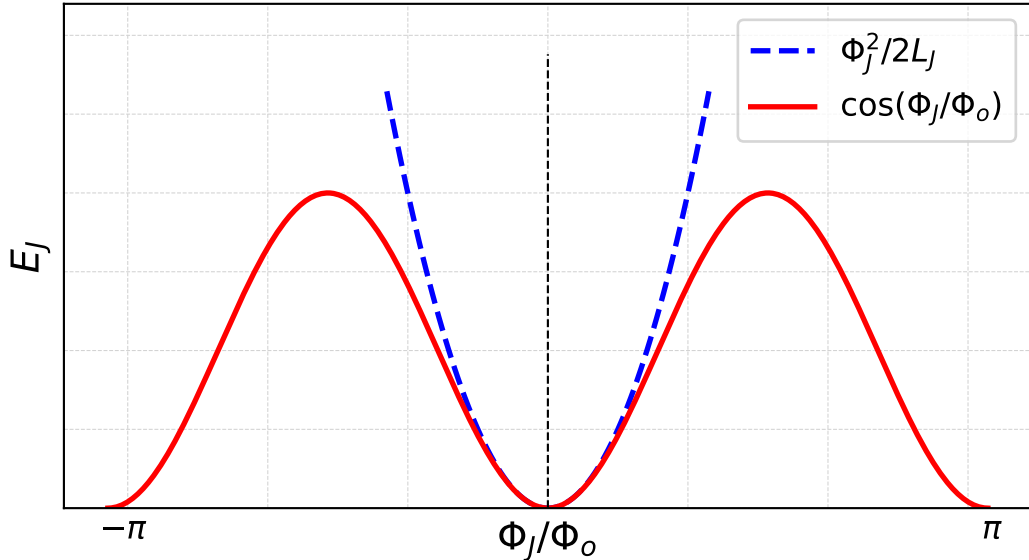


Figure 3.21: Graph representing the linear harmonic term $\{\frac{\Phi_J^2}{2L_J}\}$ - blue line} and nonlinear parts $\{-E_J \cos\left(\frac{\Phi_J}{\Phi_o}\right)\}$ - red line} in the energy description of the transmon qubit.

Transmon Hamiltonian can also be written in the Fock state basis because it is very easy to handle in such basis through making exact analogies with the Fock states of the Q.H.O. as follows:

$$\hat{H} = \hbar(\omega_o - \Delta q)\hat{N} - \frac{\hbar\alpha}{2}\hat{N}(\hat{N} - 1). \quad (3.70)$$

From the experimental point of view, if $\frac{\Phi}{\Phi_o} = 0.5$ then it means that magnetic flux is oscillating about half of the magnetic flux quantum. Similarly, if $\frac{Q_{ZPF}}{2e} \sim 1.0$ then it means that in the ground state, there is about 1 cooper pair worth of charge

fluctuating back and forth between the two SC islands. So, to avoid quantum fluctuations, we must keep the transmon at a very low temperature. Nevertheless, we cannot completely get rid of the quantum dissipation or noise in the system.

3.7 Quantum Master Equation

The previous discussion focused on pure quantum systems; however, in practical applications, we often encounter dissipation within these systems. Dissipation arises from the dephasing interaction between the pure quantum system and the environmental degrees of freedom, as well as fluctuations in the energy levels of the quantum system under consideration. The environmental degrees of freedom can include thermal vibrations or vacuum energy. In order to study the interplay of dissipation, noise, dynamics, and evolution of quantum systems, Lindblad mechanics is employed.

While the evolution of pure quantum systems is described by the well-known Schrödinger equation when considering dissipation, a quantum master equation (QME) is utilized. It is worth noting that the term "quantum master equation" is somewhat of a misnomer. QME serves as a powerful tool to address approximately 90% of the problems associated with noise in quantum systems. The general form of the QME is provided below:

$$\frac{\partial \hat{\rho}}{\partial t} = \dot{\hat{\rho}} = \frac{1}{i\hbar} [\hat{H}, \hat{\rho}] + \sum_j r_j \mathcal{L}(\hat{A}_j) \hat{\rho}. \quad (3.71)$$

Here, \mathcal{L} is the Lindblad operator/Super operator (function of operator involving the noise phenomena) operates on $\hat{\rho}$. The first part of the Von Neuman equation elaborates the coherent evolution of the system. r_j 's are the dissipation/decay rates for the different noise channels. QME is also called Lindblad Markovian quantum master equation because it deals with the Markovian processes i.e. processes that do not bother about history. Lindblad operator form is as:

$$\mathcal{L}(\hat{A}_j) \hat{\rho} = \hat{A}_j \hat{\rho} \hat{A}_j^\dagger - \frac{1}{2} \hat{A}_j^\dagger \hat{A}_j \hat{\rho} - \frac{1}{2} \hat{A}_j^\dagger \hat{\rho} \hat{A}_j. \quad (3.72)$$

Here, A_j are the relaxation operators through which the environment gets coupled to the quantum system. Now using this QME in the next example which is the main ingredient in the study of cat states which we will study in the fourth chapter.

3.7.1 QME of Transmon qubit/TLS in the presence of relaxation and dephasing

Consider Figure 3.22, which depicts a schematic representation of a two-level system utilizing the quantum master equation (QME) framework. The energy levels under consideration are denoted as $|g\rangle$ (ground state) and $|e\rangle$ (excited state). The relaxation operators associated with the system are indicated as r_- , which represents the transition rate from the excited to the ground state, r_+ , denoting the transition rate from the ground to the excited state, and r_ϕ , is the relaxation rate due to dephasing. These relaxation processes can be further elucidated in a more explicit manner:

- The transition probability rate r_- accounts for the decay of the two-level system from the excited state to the ground state.
- The transition probability rate r_+ corresponds to the transition probabilities from the ground state to the excited state and may arise due to thermal vibrations.
- The relaxation rate r_ϕ is attributable to the dephasing process, which leads to a loss of coherence in the system.

$$\hat{A}_- = |g\rangle \langle e| = \sigma_- \quad \hat{A}_+ = |e\rangle \langle g| = \sigma_+ \quad \hat{A}_\phi = \sqrt{2} |e\rangle \langle e|. \quad (3.73)$$

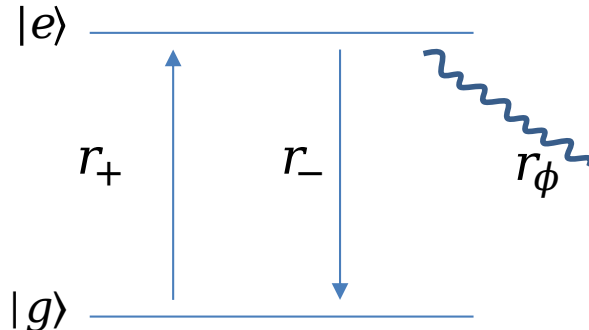


Figure 3.22: Schematic portrayal of artificial atom (two-level system here, transmon qubit) in presence of relaxation rate $= r_-$, dephasing rate $= r_\phi$, and transition rate due thermal vibration $= r_+$

Taking into account all the aforementioned relaxation processes in a general two-level system and employing the quantum master equation (QME), we can analyze the evolution of the occupation probabilities of the system in each of its two states. This analysis yields a set of equations known as the **Dissipative Bloch Equations**. These equations serve as an exact analog to the four Bloch

equations previously discussed in the context of the pure two-level system.

$$\dot{P}_{ee} = -r_- P_{ee} + r_+ P_{gg} \quad \dot{P}_{gg} = r_- P_{ee} - r_+ P_{gg}, \quad (3.74)$$

$$\dot{P}_{ge} = i\omega_{at} t P_{ge} - \left(\frac{r_+ + r_-}{2} + r_\phi \right) P_{ge} \quad \dot{P}_{eg} = \dot{P}_{ge}. \quad (3.75)$$

These four equations describe the dynamics of transmon or general artificial atoms (two-level systems) in the presence of quantum noise.

Chapter 4

A New Approach to Engineer the Kerr-cat States in Superconducting Resonators

4.1 Conceptual Overview

As we have seen in the concluding sections of the previous chapter that SC qubits have anharmonicity in their energy levels. Therefore, when SC qubits like transmon qubits are placed inside SC resonators, and their Hamiltonian is analyzed further, significant advantages arise from their nonlinear energy levels. These advantages include the ability to evolve the system into cat states, among others. However, the presence of the transmon qubit introduces a Kerr effect, specifically the self-Kerr effect, which distorts the desired cat states, as highlighted by Joo and Ginossar [86]. To mitigate this effect, a two-photon drive is employed to counteract the Kerr effect induced by the anharmonicity of energy levels of the transmon qubit, thereby enabling the generation of perfect cat states. Moreover, we have observed that these states exhibit enhanced stability against single-photon loss and dephasing effects. We have successfully implemented these states as the foundation for quantum logic. The subsequent sections delve into a comprehensive analysis of the aforementioned central theme, present the final outcomes, and provide concluding remarks.

4.1.1 Kerr effect and the Schrodinger cat states

Kerr medium is a medium whose refractive index depends upon the intensity of the light being propagated through that material. A light beam acquires phase shift while propagating through the material with a relation $\phi_{kerr} = \chi\tau I$ where

the intensity of the light beam is denoted by I , τ is the interaction time and χ is the Kerr amplitude. This effect has widely been used in nonlinear quantum optics, especially in creating an ultra-fast pulse and generating squeezed states. Similarly, its analog in the field of circuit QED is due to the nonlinear inductance of the Josephson Junction i.e. this term $\phi_4 = (b^\dagger + b)^4$ when we expand the *cosine* term of the inductance. When a qubit is coupled with any resonator, the resonator acquires an anharmonicity, behaving like a Kerr medium. SC resonators with large values of χ (actually χ/κ where κ is the single photon loss rate) show promising results, thus, creating photonic SCS.

4.2 Model a Hamiltonian of the Kerr-nonlinear Resonator

We have seen in the above sections: the Hamiltonian of the transmon qubit (in chapter 3), that exploiting the *cosine* term gives us the required nonlinearity $(b^\dagger + b)^4$ which is the source of Kerr effect in the system. Our system consists of a transmon qubit inside the resonator and the drive field.

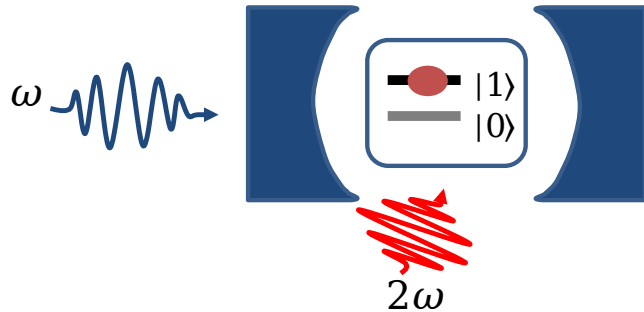


Figure 4.1: Cavity containing a transmon qubit that induces a Kerr nonlinearity in the system. The frequency of the photon drive is double the frequency of the resonator.

The Hamiltonian of a general KNR with n-photon drive field (see Fig. 4.1 which is specific to two-photon driven KNR) is given as:

$$\hat{H} = \hbar\omega_r \hat{b}^\dagger \hat{b} - \chi \hat{b}^{\dagger n} \hat{b}^n + (E_p \hat{b}^{\dagger n} e^{-in\omega_f t} + E_p^* \hat{b}^n e^{in\omega_f t}). \quad (4.1)$$

The first term corresponds to the Hamiltonian of the resonator having frequency ω_r and \hat{b} (\hat{b}^\dagger) are the annihilation (creation) operators. The second term in \hat{H} is depicting the nonlinearity we took from exploiting the Hamiltonian of the transmon qubit to the fourth-order term. In this, $\chi = \frac{\hbar\alpha}{2}$ {Eq. 3.69} is the amplitude of the nonlinearity due to the Kerr effect. The third term in the Hamiltonian represents the n-photon drive field with the frequency ω_f and drive amplitude E_p . Using the

rotating frame approach and the resonant condition ($\omega_f = \omega_r$), the Hamiltonian of the system at the resonator frequency is given by the following expression:

$$\hat{H}_{cat} = -\chi \hat{b}^{\dagger n} \hat{b}^n + E_p \hat{b}^{\dagger n} + E_p^* \hat{b}^n. \quad (4.2)$$

The given expression of the Hamiltonian is expressed in a vivid form as follows:

$$\hat{H}_{cat} = \chi \left(\hat{b}^{\dagger n} - \frac{E_p^*}{\chi} \right) \left(\hat{b}^n - \frac{E_p}{\chi} \right) + \frac{|E_p|^2}{\chi}. \quad (4.3)$$

The expression \hat{H}_{cat} depicts that we get n-coherent states $|\beta\rangle$ with amplitude $\beta^n = \frac{E_p}{\chi}$. Thus, we say that there are n-coherent states $|\beta\rangle$ that are the degenerate eigenstates of the aforementioned Hamiltonian \hat{H}_{cat} with the energy $E_n = \frac{|E_p|^2}{\chi}$. Next, we restrict our discussion to a two-photon drive, $n= 2$ (See Fig. 4.1). The Hamiltonian of the two-photon driven KNR is given as:

$$\hat{H}_{2ph} = -\chi \hat{b}^{\dagger 2} \hat{b}^2 + E_p \hat{b}^{\dagger 2} + E_p^* \hat{b}^2. \quad (4.4)$$

Derivation of the Kerr effect term χ in the Hamiltonian is extensively given in the Ph.D. dissertation of Johnson [87] {specifically equation 3.24 in the referenced thesis}. The intuition behind the system's Hamiltonian can be exploited when we draw out trajectories of the quadratures of the Hamiltonian (taken as classically). Sometimes it is called the meta-potential approach, which means plugging the classical phase space coordinates $\hat{b} = \hat{x} + i\hat{p}$ and $\hat{b}^\dagger = \hat{x} - i\hat{p}$. The figure is given in the research work of Grimm and et. al. {Fig. 1(c), [2]} which shows that the given Hamiltonian have coherent states as their degenerate eigenstates. These coherent states, whose superposition is cat state, we need them for our analysis in the dissertation.

4.2.1 Steady state of the system Hamiltonian

To study the dynamics of the given Hamiltonian, we calculate its steady state. As we know that the ME describes the evolution of the system under noise channels. Under single-photon loss, ME of the concerned system is given as:

$$\dot{\hat{\rho}} = -i[H_{eff}, \hat{\rho}] + \kappa \hat{b} \hat{\rho} \hat{b}^\dagger, \quad (4.5)$$

where $H_{eff} = \hat{H}_{2ph} - i\kappa \frac{\hat{b}^\dagger \hat{b}}{2}$ is the effective Hamiltonian and non-hermitian in nature and κ is the single photon loss rate. Applying the displacement operator on the

effective Hamiltonian, we derive it as:

$$\hat{H}'_{eff} = D^\dagger(\beta_o) \hat{H}_{eff} D(\beta_o). \quad (4.6)$$

Similarly calculating the above expression and obviating the constant terms which only give a shift in the energy spectrum of the H_{eff} , and taking the β_o terms to calculate the conditions for the amplitude of coherent state as follows:

$$-2\chi\beta_o^2\beta_o^* + 2E_p\beta_o^* - i\frac{\kappa}{2}\beta_o = 0, \quad (4.7)$$

From here, β_o must be zero or equal to $re^{i\theta}$ where

$$r = \left(\frac{4E_p^2 - \frac{\kappa^2}{4}}{4\chi^2} \right), \quad \theta = \frac{1}{2} \tan^{-1} \left(\frac{\kappa}{\sqrt{16E_p^2 - \kappa^2}} \right) \quad (4.8)$$

If we plug $\beta_o = 0$ and we observe that system becomes unstable due to large fluctuations of near resonant field drive with strength E_p . But for $\beta_o = re^{i\theta}$, the effective Hamiltonian becomes as:

$$\hat{H}'_{eff} = \frac{1}{2} \left[\frac{i\kappa\beta_o}{2\beta_o^*} + h.c. \right] - (4\chi|\beta_o|^2 + i\frac{\kappa}{2})\hat{b}^\dagger\hat{b} - \chi\hat{b}^{\dagger 2}\hat{b}^2 - 2\chi\beta_o\hat{b}^{\dagger 2}\hat{b} - 2\chi\beta_o^*\hat{b}^\dagger\hat{b}^2. \quad (4.9)$$

The first two terms in the above expression give the depiction of a parametric drive field with an amplitude $|\frac{\kappa}{2}|$ and this is detuned by the coefficient of $\hat{b}^\dagger\hat{b}$ which is approximately equal to $4\chi|\beta_o|^2$. This means that a single photon loss channel does squeeze the field drive around $\beta_o = re^{i\theta}$ which leads to an increase in the fluctuations. But for small values of $\kappa \ll 8\chi|\beta_o|^2$, the fluctuations are small enough to be ignored. Thus, single-photon loss does not account for any noticeable difference and coherent states remain the eigenstate of the effective Hamiltonian. So, $\hat{\rho} = (|\beta_o\rangle\langle\beta_o| + |-\beta_o\rangle\langle-\beta_o|)/2$ is the steady state of the master equation of resonator under loss channels.

If we expand our analysis of the system, we can see that there are two other main loss channels which are photon dephasing and two-photon loss. Under dephasing with the loss rate κ_Φ , the Lindblad ME is as:

$$\dot{\hat{\rho}} = -i[H_{eff}, \hat{\rho}] + \kappa_\Phi \hat{b}^\dagger \hat{b} \hat{\rho} \hat{b}^\dagger \hat{b}, \quad (4.10)$$

here, $H_{eff} = \hat{H}_{2ph} - i\kappa_\Phi \hat{b}^{\dagger 2}\hat{b}^2/2 - i\kappa_\Phi \hat{b}^\dagger\hat{b}/2$ with a substitution $[\hat{b}, \hat{b}^\dagger] = 1$. The second term in the effective Hamiltonian adds up to Kerr nonlinearity ($\chi - i\frac{\kappa_\Phi}{2}$) and the third term corresponds to again single-photon loss with the rate κ_Φ . As we have studied already that for $\kappa \ll 4\chi|\beta_o|^2$, the coherent states $|\pm\beta_o\rangle$ are the eigenstates of the system. The last term in the equation 4.10 refers to the resonator state

flipping from $|\beta_o\rangle$ to $|-\beta_o\rangle$ and vice versa with the rate = $\kappa_\Phi |\beta_o|^2 e^{-2|\beta_o|^2}$. This expression shows that we can achieve the exponential bit-flip suppression using these states in quantum computing by increasing the amplitude of β_o . Similarly, under the second loss channel: two-photon loss rate, the system decay pairs of photons to bath, the ME is given by:

$$\dot{\hat{\rho}} = -i[H_{eff}, \hat{\rho}] + \kappa_2 \hat{b}^2 \hat{\rho} \hat{b}^\dagger, \quad (4.11)$$

here, $\hat{H}_{eff} = \hat{H}_{2ph} - i\kappa_2 \hat{b}^\dagger \hat{b}^2 / 2$ and κ_2 is the two-photon loss rate. We see that it is a nonlinear term that also adds up to the Kerr nonlinear factor $(\chi - i\frac{\kappa_2}{2})$ and cannot account for detrimental effects on the cat states generation.

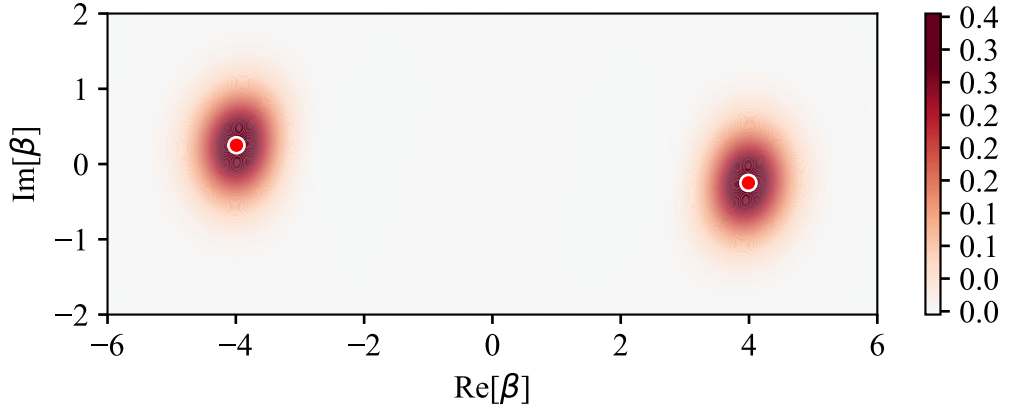


Figure 4.2: Wigner function of the steady state of the H_{eff} with $E_p = 16\chi$ where $\chi > 0$.

To plot the WF of steady state, we use the above-mentioned ME under single photon loss Eq. 4.5 and numerically integrate by using the *mesolve* function in the QuTiP package [85]. Both the figures in this section are plotted at $\frac{|\chi|}{\kappa} = 1/8$. In Figure 4.2, we use the subsequent parameters: no. of subspaces = 50, $\chi = 2.0$, $E_p = 16\chi$, $\beta_o = \sqrt{\frac{E_p}{\chi}}$, $\kappa = 16$ for making the $\frac{\chi}{\kappa} = 1/8$, $\frac{\kappa}{8|\chi\beta_o^2|} \sim \frac{1}{16}$. The fidelity (F) of the final state is 99.99%. Truncating the cavity subspaces to fewer numbers can reduce the fidelity of the final state. So far we mentioned already in Fig. 4.2 that the steady state of the system approaches the cat state. But in Figure 4.3, for $\frac{\kappa}{8|\chi\beta_o^2|} \sim \frac{1}{4}$, the cat state is distorted due to less amplitude of drive field. Thus, the fidelity is reduced to 99.91 %. Here we use these parameters: no. of subspaces = 30, $\chi = -2.0$, $E_p = 4K$, $\beta_o = \sqrt{\frac{E_p}{\chi}}$, $\kappa = 16$ for making the $\frac{\chi}{\kappa} = 1/8$. The main source of channel for the loss is still a single-photon loss, and the dephasing noise can also cause the relaxation error (bit flip error) that brings jumps between $|\beta_o\rangle$ and $|-\beta_o\rangle$.

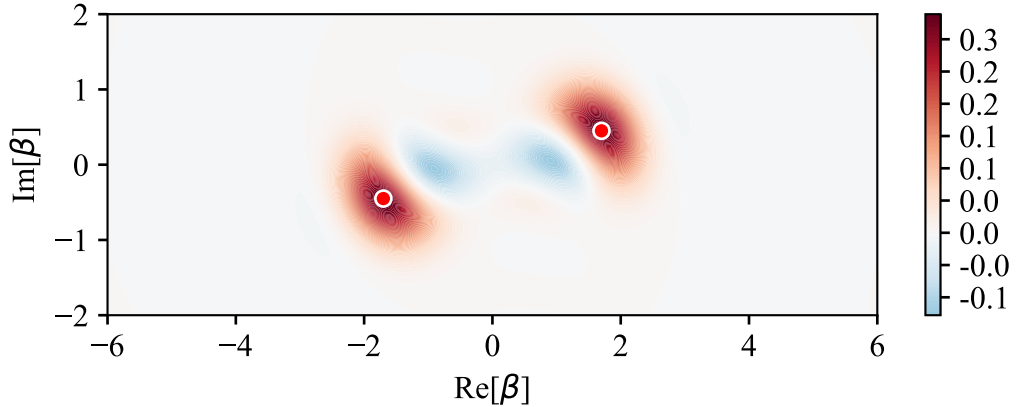


Figure 4.3: Wigner function of the steady state of the H_{eff} with $E_p = 4\chi$ where $\chi < 0$.

4.3 Preparation of Cat States

We have seen that the steady state of the effective Hamiltonian is the cat state and we can confine these states to the manifold of coherent states. But to achieve a steady state when the resonator is initialized in the resonator state, we require much time, approaching infinity. Therefore, we can take advantage of dissipation as depicted by Mirrahimi et al. [51]. But in this dissertation, we have studied that by applying an additional two-photon drive to the KNR, we can achieve the same results with better cat state preparation [58].

4.3.1 Adiabatic increase of two-photon drive

To study the dynamics of the KNR we have adiabatically increased the two-photon drive just to get rid of nonlinear effects. These effects can distort the given state if we suddenly apply the field drive on the resonator. The vacuum state and the single photon fock state are the eigenstates of an undriven KNR. When we adiabatically increase the drive field strength, these fock states of the resonator evolve to degenerate eigenstate of the KNR which are cat states. The vacuum state evolves to an even parity cat state and the single-photon fock state evolves to an odd parity cat state. Figure 4.4 shows the preparation of the cat states with the subsequent parameters: no. of subspaces = 30, $\chi = 3.0$, $E_p \sim E_{po} = 4\chi$ for $t \gg \tau$ and $\tau = 5/\chi$. In this figure, we take the single-photon loss rate $\kappa = 0$. Thus, we get the $F = 99.9\%$.

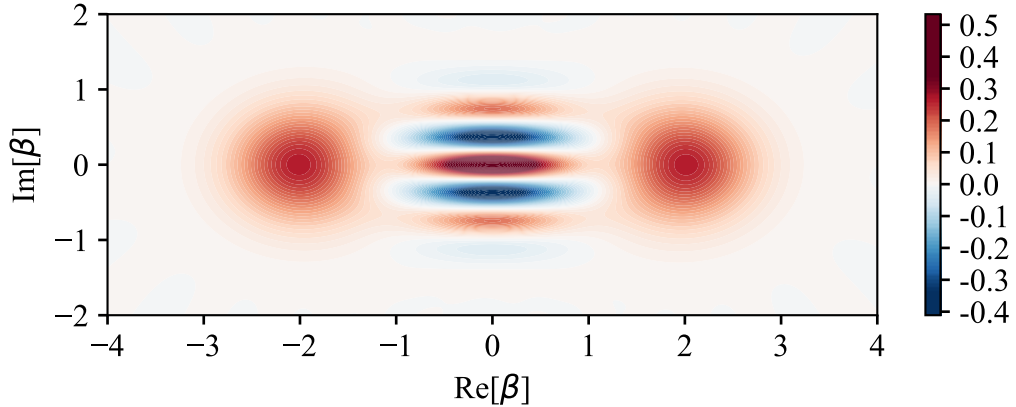


Figure 4.4: Wigner function of the cat states when \hat{H}_{2ph} of the system is evolved taking the cavity state as an initial state. The plot is taken at a time, $t = 6.5/\chi$.

In Figure 4.5, we have included the κ factor. It is clear that the final resulted cat state lost its coherence and consequently interference fringes disappear. This also confirms our discussion that the main source of the channel error is the single photon loss. Thus, we get reduced $F = 98.0\%$. To plot this figure, we use the same parameters of Fig. 4.4 here, but taking loss channels into account.

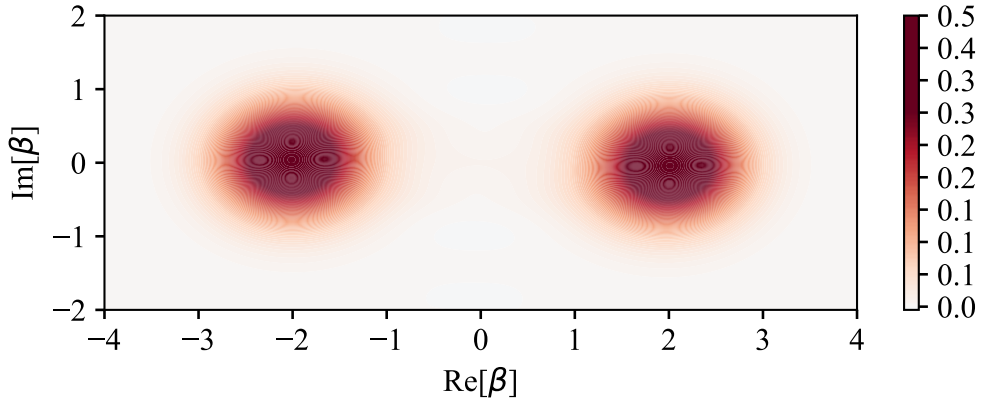


Figure 4.5: Wigner function of the cat states when \hat{H}_{2ph} of the system is evolved taking the cavity state as an initial state. The plot is taken at time $= 6.5/\chi$ and $\frac{\chi}{\kappa} = 250$.

4.3.2 Non-adiabatic initialization of the cat states

We need the final state preparation in a minimal time and we get rid of adiabaticity, slowly increasing the drive field. But when we applied the nonadiabatic/sudden electric field on the system/resonator state, we got nonlinearity and the distorted cat state as depicted in Figure 4.6. The following parameters are used to plot this figure: no. of subspaces = 30, $\chi = 3.0$, $\kappa = 0$, $E_{p0} = 4\chi$,

$$E_p = E_{po}(1 - \exp(-t^4/\tau^4)).$$

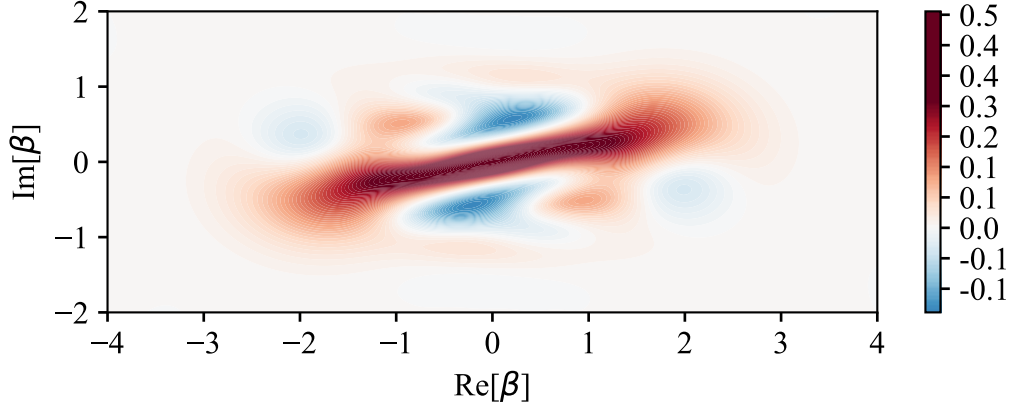


Figure 4.6: Wigner function of the state taken at time $= t = 1.37 \cdot \tau$ where $\tau = 1/\chi$. The final state is achieved when the initial state is a cavity vacuum state evolved through the H_{2ph} .

So, to counter such nonadiabatic effects, we use the approach of transitionless quantum driving [88] where we introduce a new Hamiltonian known as shortcut Hamiltonian or the driving Hamiltonian in quantum control theory that obviates the transitions in the desired state and creates the robust and perfect desired state. It counters the nonadiabatic transition during the fast evolution of the state. As our desired state is odd and even parity state, therefore, the required shortcut Hamiltonian is given by:

$$\hat{H}(t)' = i \frac{\dot{\beta}_o(t)}{N_{\beta_o(t)}^-} \left[\hat{b}^\dagger \left(|C_{\beta_o(t)}^- \rangle \langle C_{\beta_o(t)}^+| - |C_{\beta_o(t)}^+ \rangle \langle C_{\beta_o(t)}^-| \right) \hat{b} \right]. \quad (4.12)$$

To get a clearer picture of the above expression, look at time near $t = 0$, the amplitude of the coherent state is almost zero. As a result, $|C_0^+\rangle \sim |0\rangle$ and $|C_0^-\rangle \sim |1\rangle$. The expression of the Hamiltonian in terms of Fock state basis is as: $\left[\hat{b}^\dagger (|1\rangle \langle 0| - |0\rangle \langle 1|) \hat{b} \right] \sim \hat{b}^{\dagger 2} - \hat{b}^2$. Similarly, for a longer time period, these coherent states become orthogonal and the jump operator causes the transitions between odd and even photon number cat states. For large amplitude of coherent states, we approximate the above shortcut Hamiltonian in restricted coherent state basis to $(\hat{b}^{\dagger 2} - \hat{b}^2)/2\beta_o(t)$. Reconciling both the ranges 'near zero time' and 'longer time', the resulting Hamiltonian takes the following shape:

$$\hat{H}(t)' = i \frac{\dot{\beta}_o(t)}{N_{\beta_o(t)}^- [1 + 2\beta_o(t)]} (\hat{b}^{\dagger 2} - \hat{b}^2). \quad (4.13)$$

Here, $N_{\beta_o(t)}^- = \frac{1}{\sqrt{2(1-e^{-2|\beta_o|^2})}}$ is the normalization constant. For the implementation of the above-mentioned Hamiltonian, we have applied one additional two-photon

drive field E'_p that is orthogonal to the already being applied field E_p . The desired perfect cat state is shown in Fig. 4.7 after applying the required shortcut Hamiltonian.

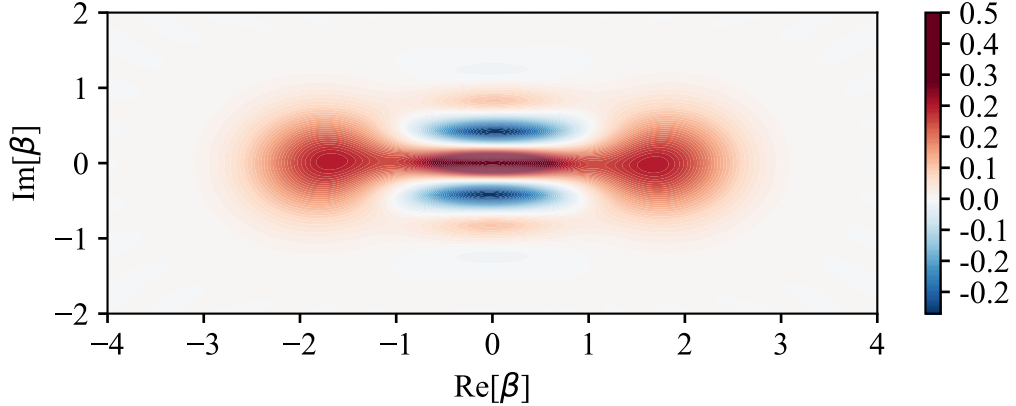


Figure 4.7: Wigner function of the state taken at time $t = 1.49\tau$ where $\tau = 1/\chi$. The state is achieved when the initial state is a cavity vacuum state evolved through the $H_{xy} = H_{2ph} + H'$. We have taken one additional drive field $E'_p = i \frac{\dot{\beta}_o(t)}{N_{\beta_o(t)}^{-}[1+2\beta_o(t)]}$ which is realization to H' . Here, the amplitude of coherent state $\beta_o = \sqrt{E_p/\chi}$

4.4 Stabilization of Kerr-cat States by using Two-Photon Drive

In the previous sections, we have generated high-fidelity cat states. Now, the cat states have been formed, we need to see if they are stabilized against the possible error channels or not. We want to see if our method i.e. two-photon drive method, can counter the phase evolution due to Kerr nonlinearity and dephasing due to single-photon or double-photon loss. As in Figure 4.8 without a two-photon drive, at $t = \frac{\pi}{8\chi}$, the states are rotated due to the Kerr nonlinearity factor. At $t = \frac{\pi}{K}$, we have a distorted cat state which can be visualized through the reduced contrast of the Wigner function and the reduced separation of the cat components. This shows that the final state isn't generated with a higher level of accuracy.

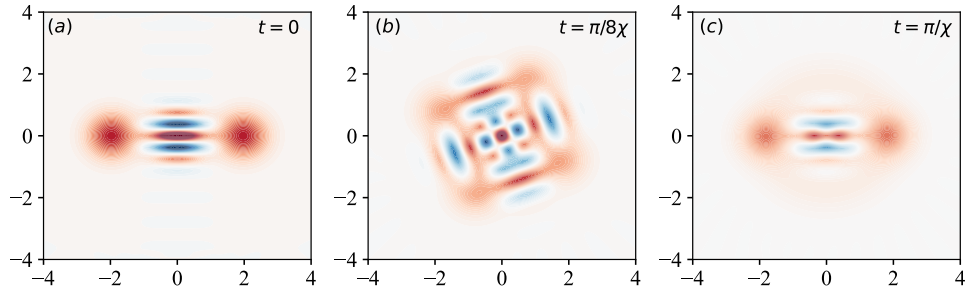


Figure 4.8: Wigner function of the states at different time scales under lossy KNR Hamiltonian. Initial state: even parity cat states $C_{\beta_o}^+$. Here x-axis = $\text{Re}[\beta_o]$ and y-axis = $\text{Im}[\beta_o]$ and probabilities scale: Most red = 0.5 and most blue = −0.4.

Applying an additional two-photon drive to the KNR in Figure 4.9, we have seen that the required cat state becomes stabilized for a longer time period and the observations such as reduced contrast in the Wigner function and reduced separation of cat components isn't more visible as was in the Figure 4.8(c).

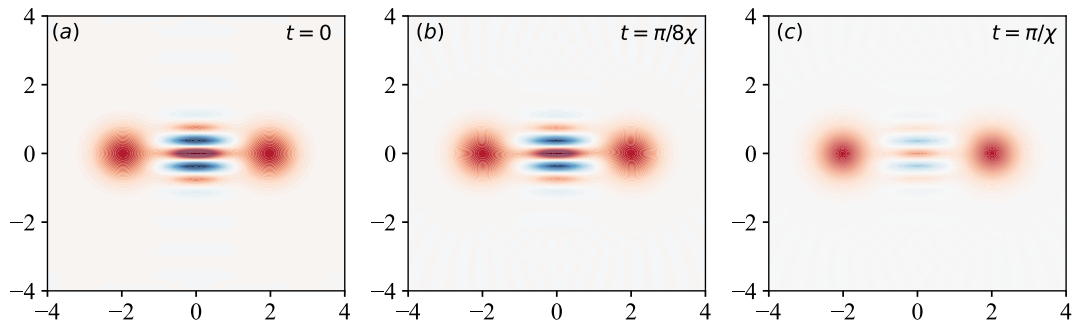


Figure 4.9: Wigner function of the states at different time scales under KNR with two-photon drive Hamiltonian. Initial state: even parity cat states $C_{\beta_o}^+$. Here x-axis = $\text{Re}[\beta_o]$ and y-axis = $\text{Im}[\beta_o]$ and probabilities scale: Most red = 0.5 and most blue = −0.4.

4.5 qcMAP gate

The detailed steps followed for the qcMAP gate are written sequentially in the literature review section (1st chapter) of this dissertation. But here, we have followed a few different steps. Here, we initialized the qubit state in a superposition of ground and excited state $\frac{|e\rangle+|g\rangle}{\sqrt{2}}$ and the resonator in the coherent state $|i\beta_o\rangle$ where its amplitude is $\beta_o = 4$ (a real quantity). The composite state of qubit and resonator evolve for a time T_{gate} under the ideal dispersive Hamiltonian $\hat{H}_{dispersive}$, the full Jaynes-Cummings Hamiltonian \hat{H}_{JC} , and the full Jaynes-Cummings Hamiltonian with a two-photon drive field \hat{H}_{2pht} . These three Hamiltonians are given as follows:

- $\hat{H}_{dispersive} = \frac{g^2}{\Delta} \hat{b}^\dagger \hat{b}$
- $\hat{H}_{JC} = \Delta \hat{\sigma}_z + g(\hat{b}^\dagger \hat{\sigma}_- + \hat{b} \hat{\sigma}_+)$
- $\hat{H}_{2pht} = \Delta \hat{\sigma}_z + g(\hat{b}^\dagger \hat{\sigma}_- + \hat{b} \hat{\sigma}_+) - (E_p \hat{b}^\dagger \hat{b}^\dagger + E_p^* \hat{b} \hat{b})$

During the evolution for T_{gate} , the resonator, and qubit get entangled and the state becomes as $|\beta_o, g\rangle + |-\beta_o, e\rangle$ (not normalized). Next, we apply the ideal displacement operator i.e. displaces the cavity state by the required amplitude, which transforms the given entangled state to a displaced entangled state $|2\beta_o, g\rangle + |0, e\rangle$. Then we apply the conditional rotation operator i.e. that rotates the given qubit state conditioned if the resonator state is a vacuum state, that disentangles the resonator from the qubit state and the composite state becomes as follows: $(|2\beta_o\rangle + |0\rangle) \otimes |g\rangle$. Then we displace the resonator state by an amplitude β_o to make it symmetric to the origin of the Wigner function by applying the displacement operator $D(-\beta_o)$. Following are the parameters, we used while plotting the Wigner functions of the final Schrodinger cat state: no. of cavity subspaces = 50, no. of qubit subspaces = 2, $\Delta = 2\pi \times 1.59$ GHz, $g = 2\pi \times 111.4$ MHz, $\kappa = 2\pi \times 7$ KHz, $\beta = 4$, $E_{po} = 2\pi \times 557$ KHz, $\phi = \pi/2$, $T_{gate} = (\pi/2) \cdot (\Delta/g^2)$, $\chi = g^4/\Delta^3$, and $\theta = \pi/2$.

We have seen that during the evolution of the composite state under JC Hamiltonian, due to the self-Kerr effect, the final cat state becomes distorted as can be visualized in the research work of Joo and Ginossar (Fig. 1(a), [86]). But when we take a two-photon drive into account, this method cancels the self-Kerr effects and consequently cancels the distortion of the final cat state and we get a final perfect cat state whose fidelity approaches unity.

4.6 Implementation of Universal Quantum Logic Gates

To use these states for the FTQC, we have to apply DiVincenzo's criteria. If these states fulfill the general requirements, then these states can be used for quantum logic. In this case, we have generated even and odd cat state preparation and we map these both cat states as the $|0\rangle$ and $|1\rangle$ as a computational basis of the new modified Bloch sphere, respectively.

4.6.1 Z gate

Z-gate is a quantum operation highly used in quantum computing and it is also referred to as Pauli-Z gate. It is a single qubit gate that operates on an individual

qubit and induces the phase shift. That is, in a Bloch sphere picture, a rotation around the Z-axis by π radians on the state of the qubit. Mathematically, the Z gate in a matrix form is represented as follows:

$$Z = \begin{bmatrix} 1 & 0 \\ 0 & -1 \end{bmatrix} \quad (4.14)$$

Following are the eigenstates and eigenvalues in a computational basis of the Z gate when it is applied to individual qubits.

$$Z |0\rangle = |0\rangle \quad Z |1\rangle = -|1\rangle \quad (4.15)$$

So, it is clear from above that this gate leaves the ground state $|0\rangle$ unaffected while induces a phase inversion (sign change) on the excited state $|1\rangle$. But, in the context of Kerr cat qubit, the Z gate is applied when we lift the degeneracy between our proposed computational basis $|0\rangle$ and $|1\rangle$ which are the degenerate eigenstates of the system Hamiltonian. This is done by using an additional single photon field drive to the H_{2ph} . The gate Hamiltonian becomes:

$$\hat{H}_z = \hat{H}_{2ph} + E_z(\hat{b}^\dagger + \hat{b}). \quad (4.16)$$

When E_p is real and $E_z \ll |4\chi\beta_o^3|$, E_z only lifts the degeneracy by $\delta_z = 4E_z\beta_o$. The Z-gate with the basis $|0\rangle$ and $|1\rangle$ will look as: $I E_z(\hat{b}^\dagger + \hat{b})$ where $I = \delta_z\sigma_z/$. On a computational basis, these operators will look like as: $I = |0\rangle\langle 0| + |1\rangle\langle 1|$ and $\sigma_z = |0\rangle\langle 0| - |1\rangle\langle 1|$.

4.6.2 NOT or X gate

In simple terms, Not gate when applied to one state, changes it to another available state. For example $X|0\rangle = |1\rangle$. So, in the case of Kerr cat states, the strong confinement of the two-component cat states makes it difficult to have population inversion. So, for the application of the X-gate $R_x(\pi/2)$, we turn off the field drive and set the system to evolve under Kerr Hamiltonian. There is another way for the implementation of the X-gate for general θ is that we introduce a detuning factor between the resonator and the two-photon drive. The corresponding Hamiltonian is: $\hat{H}_x = \hat{H}_{2ph} + \delta\hat{b}^\dagger\hat{b}$.

4.6.3 Entangling Gate

For the completion of the universal set of gates which are the main requirement to make a quantum computer, we need a realization of the entangling gate. For its application, we take two distinct resonators or two modes of single resonators and couple them through the field drive. Previously in the application of the Z-gate, the interaction term for the two resonators is as $\sigma_{z1}\sigma_{z2}$. The interaction Hamiltonian is given below:

$$\hat{H}_{zz} = \hat{H}_{01} + \hat{H}_{02} + E_{zz}(\hat{b}_1^\dagger \hat{b}_2 + \hat{b}_1 \hat{b}_2^\dagger). \quad (4.17)$$

To simplify, we consider resonators to be the same. Interaction terms in the proposed logical basis contain the bilinear coupling Hamiltonian that is expressed as $\delta_{zz}\sigma_{z1}\sigma_{z2}$ with $\delta_{zz} = 4E_z|\beta_o|^2$.

4.7 Circuit Realizations of Two-Photon Driven Kerr-nonlinear Resonator

There are some approaches by which we realize the implementation of 2ph-KNR. One such implementation is that we have to couple flux-pumped superconducting quantum interface device (fp-SQUID) with the $\lambda/4$ microwave resonator. The Kerr nonlinearity is induced by the nonlinear inductance of the fp-SQUID and the two-photon drive is realized by setting the frequency of the modulation of the flux-pump two times the resonator frequency. The other approach to its realization is by coupling a Josephson junction with the 3D superconducting microwave cavity. Here Kerr nonlinearity is induced by the nonlinear inductance of the Josephson junction and the microwave drive on the Josephson junction gives the two-photon drive. One such realization considered by Grimm et al. {Fig. 1(d), [2]} is shown in Fig. 4.10.

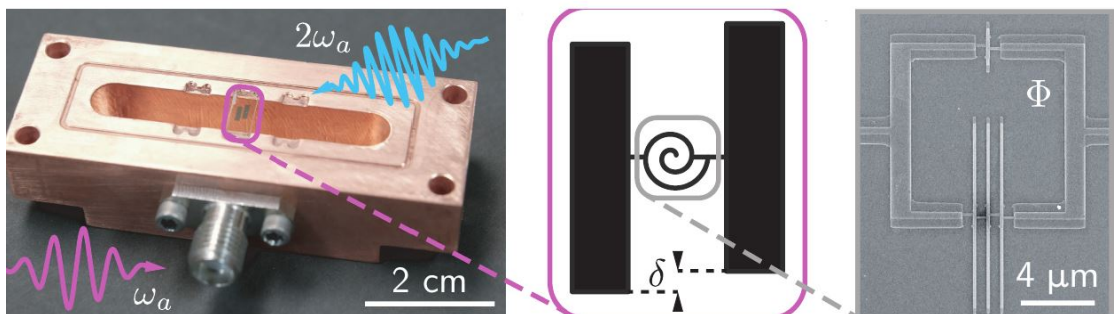


Figure 4.10: Experimental realization of the fp-SQUID integrated over the cavity. Notations of the frequencies are according to the research paper of Grimm et al. [2] but can be changed according to this dissertation.

4.8 Conclusion

To conclude, we have shown that using a two-photon drive to the KNR, we generate high-fidelity two out-of-phase superpositions of coherent states, known as SCS. These states are robust against possible loss channels. The possible error channels are single and double photon loss and dephasing effects. We have also delineated that self-Kerr effects in the qcMAP protocols are also obviated using this technique. The implementation of such a system is possible with the existing experimental technology through only the use of JPA and drive fields. In the end, we have shown the possible realization and the high-fidelity operations of the single-qubit gates and two-qubit gates using these Kerr cat qubits.

References

- [1] A. Wallraff, D. I. Schuster, A. Blais, L. Frunzio, R.-S. Huang, J. Majer, S. Kumar, S. M. Girvin, and R. J. Schoelkopf, “Strong coupling of a single photon to a superconducting qubit using circuit quantum electrodynamics,” *Nature*, vol. 431, no. 7005, pp. 162–167, 2004.
- [2] A. Grimm, N. E. Frattini, S. Puri, S. O. Mundhada, S. Touzard, M. Mirrahimi, S. M. Girvin, S. Shankar, and M. H. Devoret, “Stabilization and operation of a kerr-cat qubit,” *Nature*, vol. 584, no. 7820, pp. 205–209, 2020.
- [3] R. P. Feynman, “Simulating physics with computers,” *International Journal of Theoretical Physics*, vol. 21, pp. 467–488, June 1982.
- [4] P. Shor, “Algorithms for quantum computation: discrete logarithms and factoring,” in *Proceedings 35th Annual Symposium on Foundations of Computer Science*, pp. 124–134, 1994.
- [5] S. Boixo, S. Isakov, V. Smelyanskiy, R. Babbush, N. Ding, Z. Jiang, M. J. Bremner, J. Martinis, and H. Neven, “Characterizing quantum supremacy in near-term devices,” *Nature Physics*, vol. 14, p. 595–600, 2018.
- [6] S. Lloyd, “Universal quantum simulators,” *Science*, vol. 273, no. 5278, pp. 1073–1078, 1996.
- [7] J. Biamonte, P. Wittek, N. Pancotti, P. Rebentrost, N. Wiebe, and S. Lloyd, “Quantum machine learning,” *Nature*, vol. 549, no. 7671, pp. 195–202, 2017.
- [8] A. Aspuru-Guzik, A. D. Dutoi, P. J. Love, and M. Head-Gordon, “Simulated quantum computation of molecular energies,” *Science*, vol. 309, no. 5741, pp. 1704–1707, 2005.
- [9] E. Farhi, J. Goldstone, S. Gutmann, J. Lapan, A. Lundgren, and D. Preda, “A quantum adiabatic evolution algorithm applied to random instances of an np-complete problem,” *Science*, vol. 292, no. 5516, pp. 472–475, 2001.

- [10] P. W. Shor, “Polynomial-time algorithms for prime factorization and discrete logarithms on a quantum computer,” *SIAM review*, vol. 41, no. 2, pp. 303–332, 1999.
- [11] C. Ballance, T. Harty, N. Linke, M. Sepiol, and D. Lucas, “High-fidelity quantum logic gates using trapped-ion hyperfine qubits,” *Physical Review Letters*, vol. 117, no. 6, p. 060504, 2016.
- [12] W. Huang, C. Yang, K. Chan, T. Tanttu, B. Hensen, R. Leon, M. Fogarty, J. Hwang, F. Hudson, K. M. Itoh, *et al.*, “Fidelity benchmarks for two-qubit gates in silicon,” *Nature*, vol. 569, no. 7757, pp. 532–536, 2019.
- [13] Y. Wu, W.-S. Bao, S. Cao, F. Chen, M.-C. Chen, X. Chen, T.-H. Chung, H. Deng, Y. Du, D. Fan, *et al.*, “Strong quantum computational advantage using a superconducting quantum processor,” *Physical Review Letters*, vol. 127, no. 18, p. 180501, 2021.
- [14] P. Jurcevic, A. Javadi-Abhari, L. S. Bishop, I. Lauer, D. F. Bogorin, M. Brink, L. Capelluto, O. Günlük, T. Itoko, N. Kanazawa, *et al.*, “Demonstration of quantum volume 64 on a superconducting quantum computing system,” *Quantum Science and Technology*, vol. 6, no. 2, p. 025020, 2021.
- [15] B. Foxen, C. Neill, A. Dunsworth, P. Roushan, B. Chiaro, A. Megrant, J. Kelly, Z. Chen, K. Satzinger, R. Barends, *et al.*, “Demonstrating a continuous set of two-qubit gates for near-term quantum algorithms,” *Physical Review Letters*, vol. 125, no. 12, p. 120504, 2020.
- [16] M. Rol, F. Battistel, F. Malinowski, C. Bultink, B. Tarasinski, R. Vollmer, N. Haider, N. Muthusubramanian, A. Bruno, B. Terhal, *et al.*, “Fast, high-fidelity conditional-phase gate exploiting leakage interference in weakly anharmonic superconducting qubits,” *Physical Review Letters*, vol. 123, no. 12, p. 120502, 2019.
- [17] K. Wright, K. M. Beck, S. Debnath, J. Amini, Y. Nam, N. Grzesiak, J.-S. Chen, N. Pisenti, M. Chmielewski, C. Collins, *et al.*, “Benchmarking an 11-qubit quantum computer,” *Nature Communications*, vol. 10, no. 1, p. 5464, 2019.
- [18] X.-L. Wang, Y.-H. Luo, H.-L. Huang, M.-C. Chen, Z.-E. Su, C. Liu, C. Chen, W. Li, Y.-Q. Fang, X. Jiang, *et al.*, “18-qubit entanglement with six photons’ three degrees of freedom,” *Physical Review Letters*, vol. 120, no. 26, p. 260502, 2018.

- [19] X.-L. Wang, L.-K. Chen, W. Li, H.-L. Huang, C. Liu, C. Chen, Y.-H. Luo, Z.-E. Su, D. Wu, Z.-D. Li, *et al.*, “Experimental ten-photon entanglement,” *Physical Review Letters*, vol. 117, no. 21, p. 210502, 2016.
- [20] H.-L. Huang, X.-L. Wang, P. P. Rohde, Y.-H. Luo, Y.-W. Zhao, C. Liu, L. Li, N.-L. Liu, C.-Y. Lu, and J.-W. Pan, “Demonstration of topological data analysis on a quantum processor,” *Optica*, vol. 5, no. 2, pp. 193–198, 2018.
- [21] H.-L. Huang, Q. Zhao, X. Ma, C. Liu, Z.-E. Su, X.-L. Wang, L. Li, N.-L. Liu, B. C. Sanders, C.-Y. Lu, *et al.*, “Experimental blind quantum computing for a classical client,” *Physical Review Letters*, vol. 119, no. 5, p. 050503, 2017.
- [22] H. Wang, J. Qin, X. Ding, M.-C. Chen, S. Chen, X. You, Y.-M. He, X. Jiang, L. You, Z. Wang, C. Schneider, J. J. Renema, S. Höfling, S. Höfling, S. Höfling, C. Lu, and J.-W. Pan, “Boson sampling with 20 input photons and a 60-mode interferometer in a 10e14 -dimensional hilbert space.,” *Physical Review Letters*, vol. 123 25, p. 250503, 2019.
- [23] M. Gong, M.-C. Chen, Y. Zheng, S. Wang, C. Zha, H. Deng, Z. Yan, H. Rong, Y. Wu, S. Li, *et al.*, “Genuine 12-qubit entanglement on a superconducting quantum processor,” *Physical Review Letters*, vol. 122, no. 11, p. 110501, 2019.
- [24] Y. Ye, Z.-Y. Ge, Y. Wu, S. Wang, M. Gong, Y.-R. Zhang, Q. Zhu, R. Yang, S. Li, F. Liang, *et al.*, “Propagation and localization of collective excitations on a 24-qubit superconducting processor,” *Physical Review Letters*, vol. 123, no. 5, p. 050502, 2019.
- [25] C. Song, K. Xu, H. Li, Y.-R. Zhang, X. Zhang, W. Liu, Q. Guo, Z. Wang, W. Ren, J. Hao, *et al.*, “Generation of multicomponent atomic schrödinger cat states of up to 20 qubits,” *Science*, vol. 365, no. 6453, pp. 574–577, 2019.
- [26] A. Omran, H. Levine, A. Keesling, G. Semeghini, T. T. Wang, S. Ebadi, H. Bernien, A. S. Zibrov, H. Pichler, S. Choi, *et al.*, “Generation and manipulation of schrödinger cat states in rydberg atom arrays,” *Science*, vol. 365, no. 6453, pp. 570–574, 2019.
- [27] J. Preskill, “Quantum computing in the NISQ era and beyond,” *Quantum*, vol. 2, p. 79, 2018.
- [28] P. Krantz, M. Kjaergaard, F. Yan, T. P. Orlando, S. Gustavsson, and W. D. Oliver, “A quantum engineer’s guide to superconducting qubits,” *Applied Physics Reviews*, vol. 6, no. 2, 2019.

- [29] M. Kjaergaard, M. E. Schwartz, J. Braumüller, P. Krantz, J. I.-J. Wang, S. Gustavsson, and W. D. Oliver, “Superconducting qubits: Current state of play,” *Annual Review of Condensed Matter Physics*, vol. 11, pp. 369–395, 2020.
- [30] D. Leibfried, R. Blatt, C. Monroe, and D. Wineland, “Quantum dynamics of single trapped ions,” *Reviews of Modern Physics*, vol. 75, no. 1, p. 281, 2003.
- [31] R. Blatt and C. F. Roos, “Quantum simulations with trapped ions,” *Nature Physics*, vol. 8, no. 4, pp. 277–284, 2012.
- [32] B. E. Kane, “A silicon-based nuclear spin quantum computer,” *Nature*, vol. 393, no. 6681, pp. 133–137, 1998.
- [33] Y. He, S. Gorman, D. Keith, L. Kranz, J. Keizer, and M. Simmons, “A two-qubit gate between phosphorus donor electrons in silicon,” *Nature*, vol. 571, no. 7765, pp. 371–375, 2019.
- [34] R. Barends, J. Kelly, A. Megrant, A. Veitia, D. Sank, E. Jeffrey, T. C. White, J. Mutus, A. G. Fowler, B. Campbell, *et al.*, “Superconducting quantum circuits at the surface code threshold for fault tolerance,” *Nature*, vol. 508, no. 7497, pp. 500–503, 2014.
- [35] F. Arute, K. Arya, R. Babbush, D. Bacon, J. C. Bardin, R. Barends, R. Biswas, S. Boixo, F. G. Brandao, D. A. Buell, *et al.*, “Quantum supremacy using a programmable superconducting processor,” *Nature*, vol. 574, no. 7779, pp. 505–510, 2019.
- [36] A. Wallraff, D. I. Schuster, A. Blais, L. Frunzio, J. Majer, M. H. Devoret, S. M. Girvin, and R. J. Schoelkopf, “Approaching unit visibility for control of a superconducting qubit with dispersive readout,” *Physical Review Letters*, vol. 95, no. 6, p. 060501, 2005.
- [37] T. Yamamoto, K. Inomata, M. Watanabe, K. Matsuba, T. Miyazaki, W. D. Oliver, Y. Nakamura, and J. Tsai, “Flux-driven josephson parametric amplifier,” *Applied Physics Letters*, vol. 93, no. 4, p. 042510, 2008.
- [38] Z. Lin, K. Inomata, W. Oliver, K. Koshino, Y. Nakamura, J. Tsai, and T. Yamamoto, “Single-shot readout of a superconducting flux qubit with a flux-driven josephson parametric amplifier,” *Applied Physics Letters*, vol. 103, no. 13, p. 132602, 2013.

- [39] Z. Lin, K. Inomata, K. Koshino, W. Oliver, Y. Nakamura, J.-S. Tsai, and T. Yamamoto, “Josephson parametric phase-locked oscillator and its application to dispersive readout of superconducting qubits,” *Nature Communications*, vol. 5, no. 1, p. 4480, 2014.
- [40] H. Paik, D. I. Schuster, L. S. Bishop, G. Kirchmair, G. Catelani, A. P. Sears, B. Johnson, M. Reagor, L. Frunzio, L. I. Glazman, *et al.*, “Observation of high coherence in josephson junction qubits measured in a three-dimensional circuit qed architecture,” *Physical Review Letters*, vol. 107, no. 24, p. 240501, 2011.
- [41] J. Majer, J. Chow, J. Gambetta, J. Koch, B. Johnson, J. Schreier, L. Frunzio, D. Schuster, A. A. Houck, A. Wallraff, *et al.*, “Coupling superconducting qubits via a cavity bus,” *Nature*, vol. 449, no. 7161, pp. 443–447, 2007.
- [42] M. Reagor, W. Pfaff, C. Axline, R. W. Heeres, N. Ofek, K. Sliwa, E. Holland, C. Wang, J. Blumoff, K. Chou, *et al.*, “Quantum memory with millisecond coherence in circuit qed,” *Physical Review B*, vol. 94, no. 1, p. 014506, 2016.
- [43] A. Megrant, C. Neill, R. Barends, B. Chiaro, Y. Chen, L. Feigl, J. Kelly, E. Lucero, M. Mariantoni, P. J. O’Malley, *et al.*, “Planar superconducting resonators with internal quality factors above one million,” *Applied Physics Letters*, vol. 100, no. 11, p. 113510, 2012.
- [44] J. Koch, M. Y. Terri, J. Gambetta, A. A. Houck, D. I. Schuster, J. Majer, A. Blais, M. H. Devoret, S. M. Girvin, and R. J. Schoelkopf, “Charge-insensitive qubit design derived from the cooper pair box,” *Physical Review A*, vol. 76, no. 4, p. 042319, 2007.
- [45] J. A. Schreier, A. A. Houck, J. Koch, D. I. Schuster, B. R. Johnson, J. M. Chow, J. M. Gambetta, J. Majer, L. Frunzio, M. H. Devoret, *et al.*, “Suppressing charge noise decoherence in superconducting charge qubits,” *Physical Review B*, vol. 77, no. 18, p. 180502, 2008.
- [46] D. A. Lidar and T. A. Brun, *Quantum error correction*. Cambridge university press, 2013.
- [47] E. T. Campbell, B. M. Terhal, and C. Vuillot, “Roads towards fault-tolerant universal quantum computation,” *Nature*, vol. 549, no. 7671, pp. 172–179, 2017.
- [48] A. Y. Kitaev, “Fault-tolerant quantum computation by anyons,” *Annals of Physics*, vol. 303, no. 1, pp. 2–30, 2003.

- [49] P. W. Shor, “Scheme for reducing decoherence in quantum computer memory,” *Physical Review A*, vol. 52, no. 4, p. R2493, 1995.
- [50] D. Gottesman, A. Kitaev, and J. Preskill, “Encoding a qubit in an oscillator,” *Physical Review A*, vol. 64, no. 1, p. 012310, 2001.
- [51] M. Mirrahimi, Z. Leghtas, V. V. Albert, S. Touzard, R. J. Schoelkopf, L. Jiang, and M. H. Devoret, “Dynamically protected cat-qubits: a new paradigm for universal quantum computation,” *New Journal of Physics*, vol. 16.
- [52] D. Aharonov and M. Ben-Or, “Fault-tolerant quantum computation with constant error,” in *Proceedings of the twenty-ninth annual ACM symposium on Theory of computing*, pp. 176–188, 1997.
- [53] E. Knill, R. Laflamme, and W. H. Zurek, “Resilient quantum computation: error models and thresholds,” *Proceedings of the Royal Society of London. Series A: Mathematical, Physical and Engineering Sciences*, vol. 454, no. 1969, pp. 365–384, 1998.
- [54] P. Aliferis, D. Gottesman, and J. Preskill, “Quantum accuracy threshold for concatenated distance-3 codes,” *Quantum Info. Comput.*, vol. 6, p. 97–165, mar 2006.
- [55] A. Javadi-Abhari, P. Gokhale, A. Holmes, D. Franklin, K. R. Brown, M. Martonosi, and F. T. Chong, “Optimized surface code communication in superconducting quantum computers,” in *Proceedings of the 50th Annual IEEE/ACM International Symposium on Microarchitecture*, pp. 692–705, 2017.
- [56] S. Puri, L. St-Jean, J. A. Gross, A. Grimm, N. E. Frattini, P. S. Iyer, A. Krishna, S. Touzard, L. Jiang, A. Blais, *et al.*, “Bias-preserving gates with stabilized cat qubits,” *Science Advances*, vol. 6, no. 34, p. eaay5901, 2020.
- [57] R. Lescanne, *Engineering multi-photon dissipation in superconducting circuits for quantum error correction*. Theses, Université Paris sciences et lettres, Feb. 2020.
- [58] S. Puri, S. Boutin, and A. Blais, “Engineering the quantum states of light in a kerr-nonlinear resonator by two-photon driving,” *npj Quantum Information*, vol. 3, no. 1, p. 18, 2017.

- [59] Z. Leghtas, G. Kirchmair, B. Vlastakis, M. H. Devoret, R. J. Schoelkopf, and M. Mirrahimi, “Deterministic protocol for mapping a qubit to coherent state superpositions in a cavity,” *Physical Review A*, vol. 87, no. 4, p. 042315, 2013.
- [60] B. C. Sanders, “Entangled coherent states,” *Physical Review A*, vol. 45, no. 9, p. 6811, 1992.
- [61] J. Joo, W. J. Munro, and T. P. Spiller, “Quantum metrology with entangled coherent states,” *Physical Review Letters*, vol. 107, no. 8, p. 083601, 2011.
- [62] Y. Zhang, X. Li, W. Yang, and G. Jin, “Quantum fisher information of entangled coherent states in the presence of photon loss,” *Physical Review A*, vol. 88, no. 4, p. 043832, 2013.
- [63] S. J. van Enk and O. Hirota, “Entangled coherent states: Teleportation and decoherence,” *Physical Review A*, vol. 64, no. 2, p. 022313, 2001.
- [64] B. C. Sanders, “Review of entangled coherent states,” *Journal of Physics A: Mathematical and Theoretical*, vol. 45, no. 24, p. 244002, 2012.
- [65] C. Wang, Y. Y. Gao, P. Reinhold, R. W. Heeres, N. Ofek, K. Chou, C. Axline, M. Reagor, J. Blumoff, K. Sliwa, *et al.*, “A schrödinger cat living in two boxes,” *Science*, vol. 352, no. 6289, pp. 1087–1091, 2016.
- [66] C. Flühmann, T. L. Nguyen, M. Marinelli, V. Negnevitsky, K. Mehta, and J. Home, “Encoding a qubit in a trapped-ion mechanical oscillator,” *Nature*, vol. 566, no. 7745, pp. 513–517, 2019.
- [67] N. Ofek, A. Petrenko, R. Heeres, P. Reinhold, Z. Leghtas, B. Vlastakis, Y. Liu, L. Frunzio, S. Girvin, L. Jiang, *et al.*, “Extending the lifetime of a quantum bit with error correction in superconducting circuits,” *Nature*, vol. 536, no. 7617, pp. 441–445, 2016.
- [68] R. Lescanne, M. Villiers, T. Peronnin, A. Sarlette, M. Delbecq, B. Huard, T. Kontos, M. Mirrahimi, and Z. Leghtas, “Exponential suppression of bit-flips in a qubit encoded in an oscillator,” *Nature Physics*, vol. 16, no. 5, pp. 509–513, 2020.
- [69] D. Schuster, A. A. Houck, J. Schreier, A. Wallraff, J. Gambetta, A. Blais, L. Frunzio, J. Majer, B. Johnson, M. Devoret, *et al.*, “Resolving photon number states in a superconducting circuit,” *Nature*, vol. 445, no. 7127, pp. 515–518, 2007.

- [70] L. Davidovich, A. Maali, M. Brune, J. Raimond, and S. Haroche, “Quantum switches and nonlocal microwave fields,” *Physical Review Letters*, vol. 71, no. 15, p. 2360, 1993.
- [71] S. E. Nigg, H. Paik, B. Vlastakis, G. Kirchmair, S. Shankar, L. Frunzio, M. Devoret, R. Schoelkopf, and S. Girvin, “Black-box superconducting circuit quantization,” *Physical Review Letters*, vol. 108, no. 24, p. 240502, 2012.
- [72] L. Lutterbach and L. Davidovich, “Production and detection of highly squeezed states in cavity qed,” *Physical Review A*, vol. 61, no. 2, p. 023813, 2000.
- [73] M. Wolinsky and H. Carmichael, “Quantum noise in the parametric oscillator: from squeezed states to coherent-state superpositions,” *Physical Review Letters*, vol. 60, no. 18, p. 1836, 1988.
- [74] L. Krippner, W. Munro, and M. Reid, “Transient macroscopic quantum superposition states in degenerate parametric oscillation: Calculations in the large-quantum-noise limit using the positive p representation,” *Physical Review A*, vol. 50, no. 5, p. 4330, 1994.
- [75] E. E. Hach III and C. C. Gerry, “Generation of mixtures of schrödinger-cat states from a competitive two-photon process,” *Physical Review A*, vol. 49, no. 1, p. 490, 1994.
- [76] L. Gilles, B. Garraway, and P. Knight, “Generation of nonclassical light by dissipative two-photon processes,” *Physical Review A*, vol. 49, no. 4, p. 2785, 1994.
- [77] Z. Leghtas, G. Kirchmair, B. Vlastakis, R. J. Schoelkopf, M. H. Devoret, and M. Mirrahimi, “Hardware-efficient autonomous quantum memory protection,” *Physical Review Letters*, vol. 111, no. 12, p. 120501, 2013.
- [78] P. Brooks, A. Kitaev, and J. Preskill, “Protected gates for superconducting qubits,” *Physical Review A*, vol. 87, no. 5, p. 052306, 2013.
- [79] D. A. Lidar, I. L. Chuang, and K. B. Whaley, “Decoherence-free subspaces for quantum computation,” *Physical Review Letters*, vol. 81, no. 12, p. 2594, 1998.
- [80] G. Kirchmair, B. Vlastakis, Z. Leghtas, S. E. Nigg, H. Paik, E. Ginossar, M. Mirrahimi, L. Frunzio, S. M. Girvin, and R. J. Schoelkopf, “Observation of quantum state collapse and revival due to the single-photon kerr effect,” *Nature*, vol. 495, no. 7440, pp. 205–209, 2013.

- [81] J. Guillaud and M. Mirrahimi, “Repetition cat qubits for fault-tolerant quantum computation,” *Physical Review X*, vol. 9, no. 4, p. 041053, 2019.
- [82] C. Chamberland, K. Noh, P. Arrangoiz-Arriola, E. T. Campbell, C. T. Hann, J. Iverson, H. Putterman, T. C. Bohdanowicz, S. T. Flammia, A. Keller, *et al.*, “Building a fault-tolerant quantum computer using concatenated cat codes,” *PRX Quantum*, vol. 3, no. 1, p. 010329, 2022.
- [83] Y.-H. Kang, Y. Xiao, Z.-C. Shi, Y. Wang, J.-Q. Yang, J. Song, and Y. Xia, “Effective implementation of nonadiabatic geometric quantum gates of cat-state qubits using an auxiliary qutrit,” *New Journal of Physics*, vol. 25, no. 3, p. 033029, 2023.
- [84] S. Kwon, S. Watabe, and J.-S. Tsai, “Autonomous quantum error correction in a four-photon kerr parametric oscillator,” *npj Quantum Information*, vol. 8, no. 1, p. 40, 2022.
- [85] J. R. Johansson, P. D. Nation, and F. Nori, “Qutip: An open-source python framework for the dynamics of open quantum systems,” *Computer Physics Communications*, vol. 183, no. 8, pp. 1760–1772, 2012.
- [86] J. Joo and E. Ginossar, “Efficient scheme for hybrid teleportation via entangled coherent states in circuit quantum electrodynamics,” *Scientific Reports*, vol. 6, no. 1, p. 26338, 2016.
- [87] B. R. Johnson, *Controlling photons in superconducting electrical circuits*. Yale University, 2011.
- [88] M. V. Berry, “Transitionless quantum driving,” *Journal of Physics A: Mathematical and Theoretical*, vol. 42, no. 36, p. 365303, 2009.